SAPIENZA
UNIVERSITÀ DI ROMA

Simulations and measurements of coupling impedance for modern particle accelerator devices

Facoltà di ingegneria Civile e Industriale

Corso di Laurea in Ingegneria Elettrotecnica

Candidate

Diego Ferrazza
ID number 1589942

Thesis Advisor

Prof. A.Mostacci

Co-Advisors

Dr. B.Salvant
Dr. N.Biancacci

Academic Year 2015/2016

Thesis defended on 26 October 2016
in front of a Board of Examiners composed by:

Prof. Federico Attilio Caricchi (chairman)
Prof. Sangiovanni Silvia
Prof. Maradei Francescaromana

Simulations and measurements of coupling impedance for modern particle accelerator devices
Bachelor thesis. Sapienza – University of Rome

This thesis has been typeset by LaTeX and the Sapthesis class.

Author's email: ferrazza.1589942@studenti.uniroma1.it

Contents

List of Figures

Acronyms

PS Proton synchrotron
SPS Super proton synchrotron
PEC Perfect electric conductor
ε Electric permittivity of the material
μ Magnetic permeability of the material
l Length
a Radius
FCC Future circular collider
LHC Large hadron collider
EM Electromagnetic
RRR Residual resistance ratio
v Relative velocity
c Speed of the light
β Is the ratio $\frac{v}{c}$
DUT Device under test
S-Parameter Scattering parameters
E Electric field
$\frac{B}{\mu}$ Magnetic field

Dedicato al
mio padrino

Abstract

In this document it has been treated the study of the coupling impedance in modern devices, already installed or not, in different particle accelerators. In the specific case:

- For a device in-phase of project, several simulations for impedance calculation have been done.
- For a component already realized and used, measurements of coupling impedance value have been done.

Simulations are used to determine the impact of the interconnect between to magnets, designed for the future particle accelerator FCC, on the overall impedance of the machine which is about 100 km long. In particular has been done a check between theory, simulations and measurements of components already built, allowing a better and deeper study of the component we have analysed. Controls that probably will be helpful to have a clear guideline in future works. The measurements instead concern in an existing component that was already used in LHC, the longest particle accelerator ever realised on the planet, 27 km long. The coupling impedance measurements, in that case, have been carried out to determine the real influence that the beam particle has on the material around it self. Material that may have changed some of its main properties after many hours of work. The study drove by Diego Ferrazza with the help of the entire research team BE-ABP-HSC and especially thanks to the constant presence of my two supervisors: Benoit Salvant and Nicolò Biancacci. Without forgetting the remote supervision of my thesis advisor: Prof. Andrea Mostacci.

Estratto

In questo documento viene trattato lo studio dell'impedenza di accoppiamento in dispositivi tecnologici, già istallati e non, in differenti acceleratori di particelle. Nel caso specifico vengono effettuate:

- Per un componente ancora in fase di progetto simulazioni per il calcolo dell'impedenza.
- Per un componente già realizzato ed utilizzato misure del valore di impedenza di accoppiamento.

Le simulazioni servono per determinare l'impatto che il connettore tra due magneti, progettato per il futuro acceleratore di particelle FCC, ha sull'impedenza complessiva del macchinario lungo circa 100 km. In particolare è stata fatta una verifica tra teoria, simulazioni e misure reali di componenti già realizzati, consentendo di studiare al meglio e approfonditamente il nostro componente. Controlli che eventualmente serviranno per avere una linea guida più chiara nei lavori futuri. Le misure invece riguardano un componente esistente e già utilizzato nell'LHC che al momento è il più grande acceleratore di particelle sul pianeta, lungo 27 km. Le misure di impedenza di accoppiamento, in tal caso, sono state effettuate per determinare la reale influenza che il fascio di particelle ha sul materiale che lo circonda. Materiale che può aver cambiato alcune delle sue principali proprietà dopo molte ore di lavoro. Studio realizzato da Diego Ferrazza con l'aiuto di tutto il team di ricerca BE-ABP-HSC e specialmente grazie alla costante presenza dei miei due supervisori: Benoit Salvant e Nicolò Biancacci. Senza dimenticare la supervisione in remoto del mio relatore, il prof. Andrea Mostacci.

Acknowledgments

Dopo questo bellissimo ma intenso periodo di tre anni sto coronando il mio sogno. Finalmente davanti il mio nome potrà esser scritto "ing". Un' abbreviazione che sta ad indicare un tutt'altro che "breve" impegno durante il corso di questi studi. Sarei un egoista nel dire di esser arrivato solo a questo mio primo traguardo. Perciò vorrei ringraziare le persone che mi hanno sostenuto ed aiutato sia in ambito universitario che non, ma che comunque hanno contribuito appieno allo scopo finale. Senza nessuna vergogna posso dire che la persona che più mi stata vicino è mia madre, che pazientemente mi ha ascoltato ogni qual volta lo richiedevo, essendo in grado di darmi anche ottimi consigli qualora ce ne fosse stato bisogno. Un ringraziamento non meno importante va a mio padre e mio fratello che cervavano di non rientrare a casa evitando, cosi, di distogliermi dallo studio. Vorrei salutare e dire grazie al presidente della società ASD pallavolo Segni 2000, che, con allennamenti mirati, mi ha permesso di scaricare la tensione accumulata in vista degli esami. Ora i ringraziamenti vanno ad un uomo veramente gentile e disponibile, senza il quale non avrei potuto scrivere questo lavoro: il prof.Andrea Mostacci. Seguendo il suo consiglio ho partecipato ad un tirocinio estivo indimenticabile presso il laboratorio CERN di Ginevra. Il lavoro fatto durante questo tirocinio di 12 *settimane è proprio riportato passo passo nella tesi. Durante questa esperienza sono stato seguito costantemente da due persone che veramente amano e vivono sempre in modo solare ogni ora lavorativa, trasmettendo questa voglia di fare a qualsiasi persona si trovi in quel momento al loro fianco. Dico quindi grazie ai miei due supervisori al CERN: Benoit Salvant e Nicolò Biancacci. Non sono però stati gli unici ad essere sempre disponibili, per questo sono veramente riconoscente a tutto il gruppo di ragazzi italiani che lavorava nel mio stesso stabile e che nel momento del bisogno, dopo essere stato minacciato con un coltello dal vicino di casa, insieme a Benoit e Nicolò, si sono mobilitati per trovarmi un nuovo alloggio. Quindi mi sembra giusto ringraziare anche il mio successivo coinquilino Francesco Di Lorenzo, ragazzo molto disponibile, che ha condiviso con me la casa per* 11 *settimane. Un ultimo grazie, ma assolutamente non per importanza, va ad una ragazza con cui condivido tanto della mia vita ormai da un pò di tempo. Lei è sempre stata la prima ad appoggiare le mie scelte quando c'è stata la necessità di farlo, compresa l'esperienza al CERN. Grazie.*

Chapter 1

CERN lab introduction and its accelerators

The CERN' laboratory that situates in Geneva, is one of the most important physics labs in international environment, where people constantly work for future discoveries and to overreach the boundaries of our knowledge and find new and different shapes of the particle still unknown. The member states of CERN are Austria, Belgium, Bulgaria, the Czech Republic, Denmark, Finland, France, Germany, Greece, Hungary, Israel, Italy, the Netherlands, Norway, Poland, Portugal, Romania, Slovakia, Spain, Sweden, Switzerland and the United Kingdom. Serbia is an associate member in pre-stage to membership. India, Japan, the Russian Federation, the United States of America, Turkey, the European Commission and UNESCO have observer status. Therefore CERN is an Europeans family but enlarged to the international environment.

1.1 Accelerators chain

The CERN accelerators chain or complex was shown in Figure 1.1

The overall process of the beams was shown step by step below: The protons for the experiments are taken from a bottle of hydrogen atoms. The protons are then accelerated in the Linac 2 to the kinetic energy $T = 50\ MeV$. The second step is the extraction of the beam from the Linac 2 and the next injection in the Booster (first ring accelerator) so the intense beams arrive to 1.4 GeV. After that the same extraction and injection process is done to feed the PS, thus to provide high intensity beams up to 25 GeV. Particles are then injected in the SPS so the energy at the end of acceleration is near to 450 GeV and immediately after injected in LHC, the largest particle accelerator at our days. The particles in LHC are forward in opposite directions until the energy is increased to 13 TeV and the beams are brought to collision. This is the process used still today but in a not far future the collision will be done with higher energy than the LHC, the FCC.

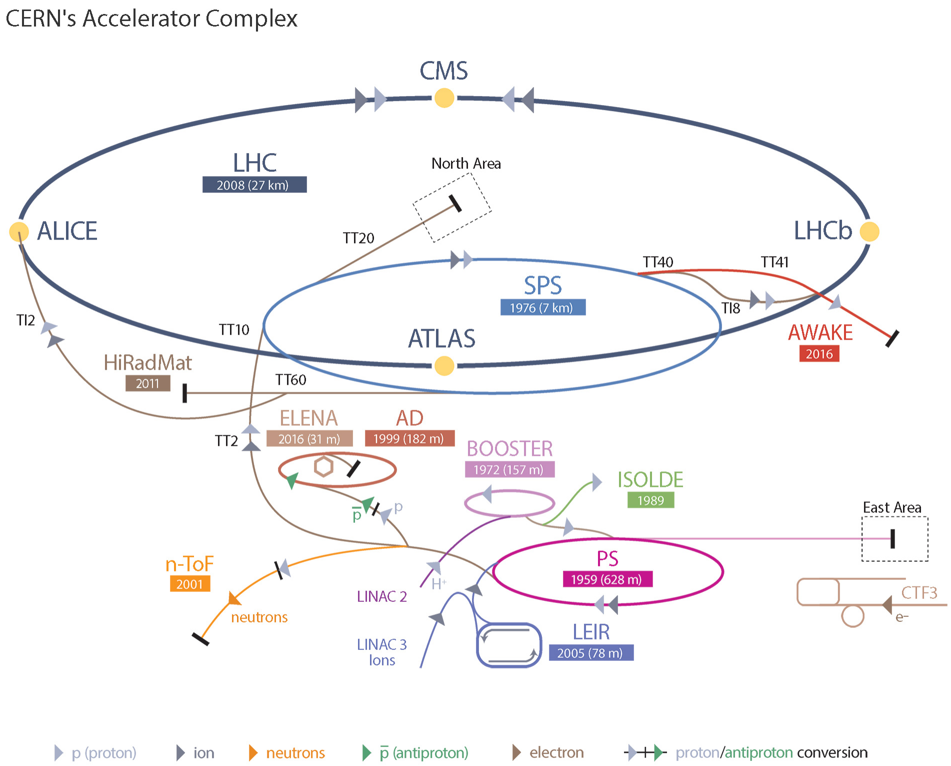

Figure 1.1. Accelerators chain by Science and Technology Facilities Council

1.2 FCC particle accelerator

The FCC "Future circular collider" will be the new and main particle accelerator of the whole chain of accelerators at CERN. This machine will be the largest accelerator of the world and will be hosted by the CERN lab that already foresees an international collaboration for its construction. The total circular length is astonishing: Figure 1.2 shows about 100 km [1] where, like in LHC there will be two different rings, one for a clockwise and the other one for counterclockwise run of the beam. The purpose of both rings is the collision in big experiments inside the FCC.

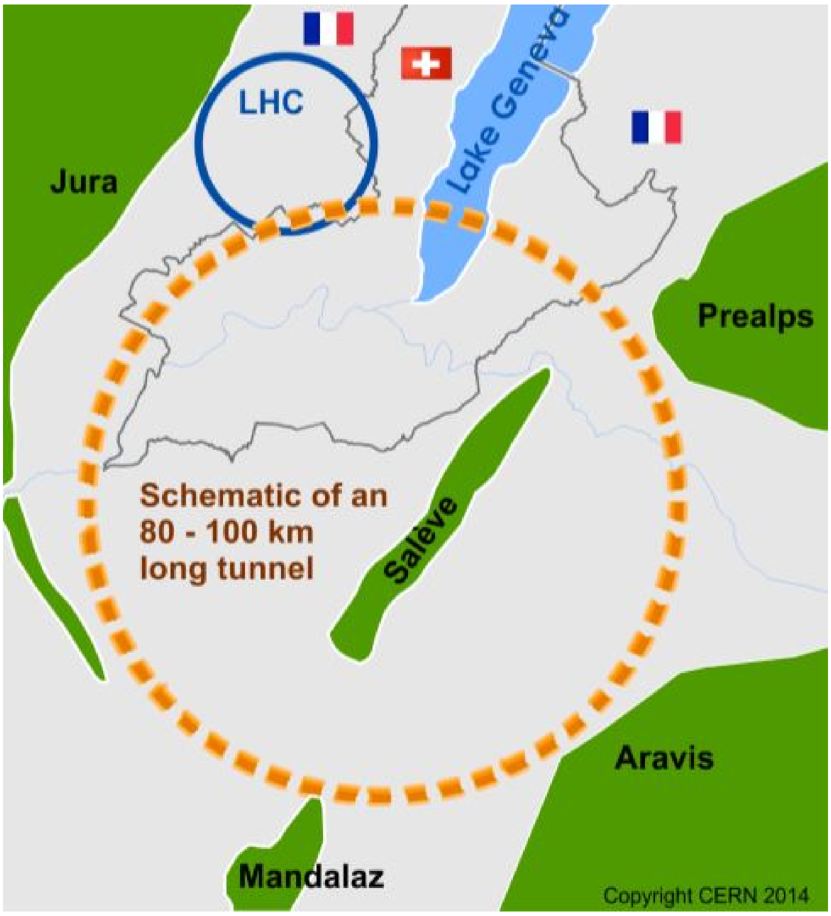

Figure 1.2. Probable FCC tunnel infrastructure Cern FCC publications

Probably the usual question is: how long will the construction last and when will be the first collision in one of the experiments? The answers are show below in a figure which explains approximately the time that CERN people need to finish it: Figure 1.3

Another important and spectacular novelty about this machine will be the energy reached during the beams running, 100 TeV (due from the collision between h-h, e-e or e-h particles) versus the 13 TeV max obtained in the LHC experiment, in this way we will discover more energetic particles than those discovered until now. When there will be the injection in the FCC, the LHC will be the last acceleration step before the injection in it. This brief presentation was made to introduce the

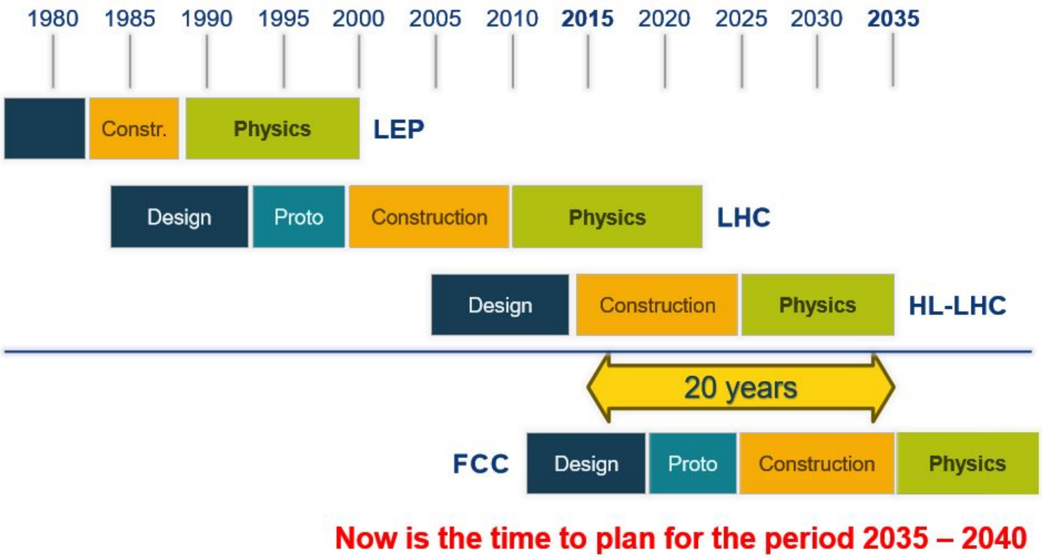

Figure 1.3. Work plane by CERN FCC publications

component studied in this thesis.

Chapter 2

Interconnect between two magnets and concerning data

The interconnect between two magnets is the subject analysed in this research. The purpose of the superconductive magnets outside this element is to turn the particles inside the FCC so that the beam will follow the trend of the ring during all the revolution time. Thus this interconnect is the junction that will allow this bunches run. The studies have been done trough the simulation to discover the losses. In particular the part under exam for the study of the impedance is the beam screen cooper, the first material that the beam meets after the vacuum. The thickness of this beam screen is very little, in particular the max penetration of the electromagnetic field inside the material is called skin-depth Figure 2.5 that is the most important parameter for the real thickness definition. The whole design of this component was reconstructed by the data shown below: Figure 2.1

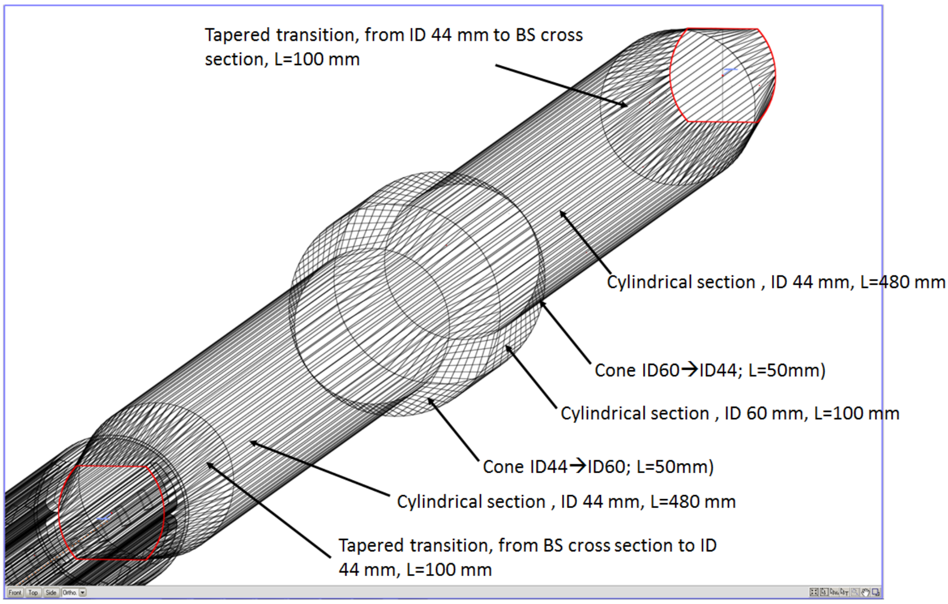

Figure 2.1. Component dimensions

In particular the real cross section of the total FCC pipe is: Figure 2.2

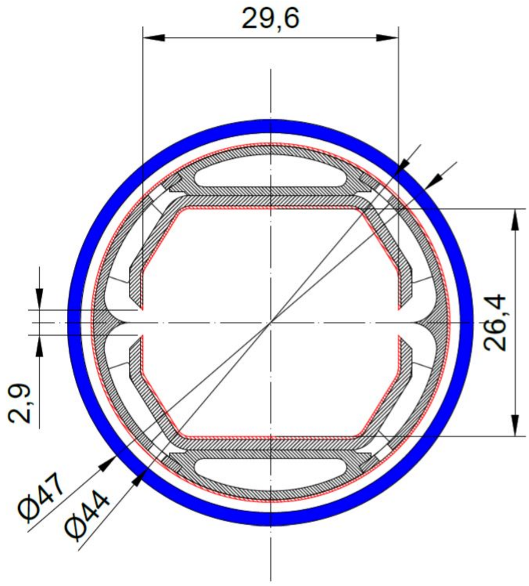

Figure 2.2. Real cross section

Thanks to the help of the mechanic CAD (AutoCad) Figure 2.3 the entrance and the exit of the interconnect for points was reconstructed. After that the whole element has been designed in electromagnetic field CAD (CST) Figure 2.4 and other important data for the study were used: Figure 2.5

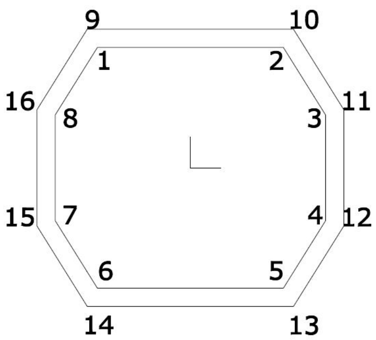

	X	Y
1	-10.185	13.2
2	10.185	13.2
3	14.8	5.8
4	14.8	-5.8
5	10.185	-13.2
6	-10.185	-13.2
7	-14.8	-5.8
8	-14.8	5.8
9	-11.295	15.2
10	11.295	15.2
11	16.8	6.38
12	16.8	-6.38
13	11.295	-15.2
14	-11.295	-15.2
15	-16.8	-6.38
16	-16.8	6.38

Figure 2.3. Cross section Autocad reconstructed

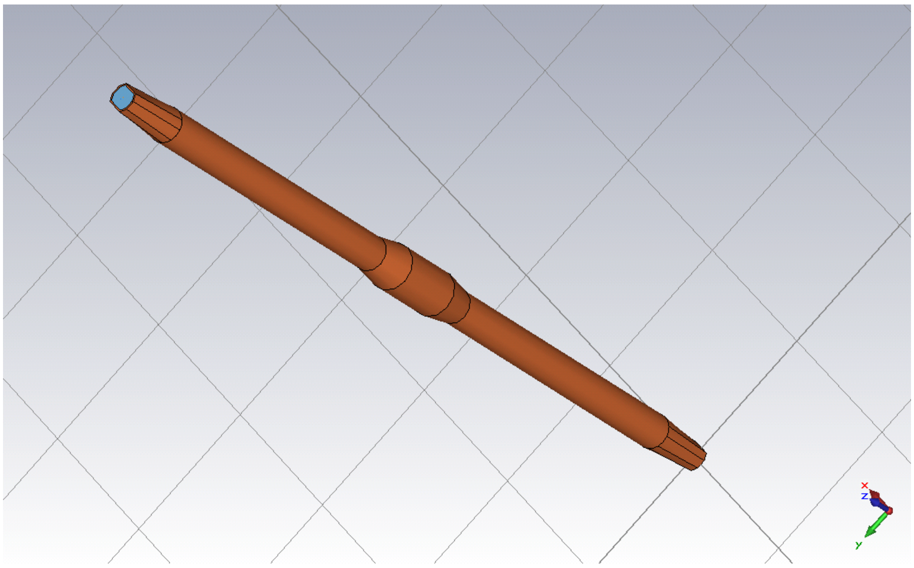

Figure 2.4. Whole component CST reconstructed

Material	$\rho(50K)$ $[\Omega \cdot m]$	Thickness [mm]
Copper (annealed)	$0.75 \cdot 10^{-9}$	0.3

Figure 2.5. Data sheet

Chapter 3

Kinds of modes studied with the help of Eigenmode CST simulations.

In this chapter it was treated the study of the modes, which are the different electromagnetic waves that can propagate or resonate respectively in wave guides or in cavities [2]. The work is mainly focused on the component under exam and the resonance modes due to the shape of it. Several verifications with some approximations, thanks to simpler structures, have been done. The cylindrical approximation will be treated even analytically. These simplification are due to the fact that in some places the interconnect is symmetric.

3.1 Analytic calculation of the modes

3.1.1 Brief introduction for the resonance frequencies

From the dimensions defined before and the shape of this element, after several simulations, the best approximation of the interconnect was found. How we can see from the interconnect design Figure 3.1, the central zone seen along z direction, has a larger radius than whole component. The EM fields excited from the travelling beam will recognise this specific part as a cavity. The cavities from this view point aren't acceleration cavity of the beam, but passive structures. This big radius was designed as a shield for the synchrotron radiation (the synchrotron radiation has not been treated in this thesis). The fact that we have a larger radius in the centre provide lower resonators frequencies than the resonances frequencies of the same interconnect that has to be supposed with 22 mm of radius. In correspondence of the resonator frequency, impedance peaks will be obtained (the impedance will be explain in the next chapter). How mentioned before the resonance frequencies are strongly depending from the geometry of the elements, when the radius increase the module of the frequencies, related to the resonant modes, decreases [2]. Having impedance spike near the low frequency is the same as having power losses peaks, these spikes are the limit for the real frequencies work range (broad-band). Thanks to the concepts just presented the first geometry that starts resonating is the cavity.

Successively for larger frequencies the long sections of the interconnect begin to resonate.

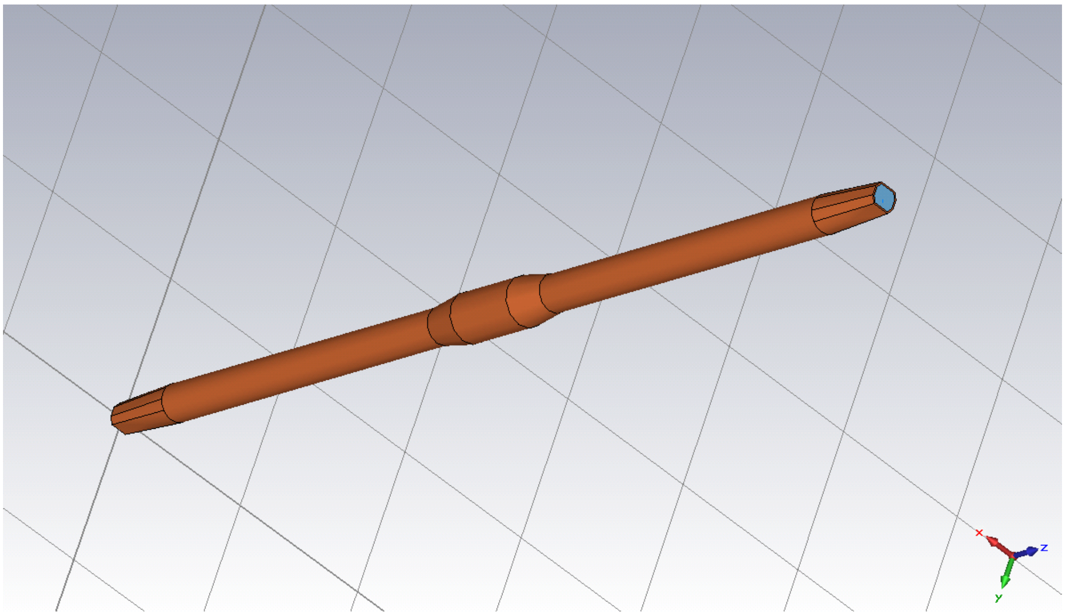

Figure 3.1. Interconnect design

3.1.2 Analytic formula for cylindrical cavity

The brief introduction is supposed to explain the first approximations that has been done, changing the whole interconnect with a perfect cylindrical cavity with dimensions length: $l = 200\ mm$ and radius $a = 30\ mm$. It is a simple and good closeness of the interconnect and can be even verified in analytic way [2] like:

For the TM modes (3.1):

$$f_{res} = \frac{1}{2\pi\sqrt{\mu\varepsilon}} \cdot \sqrt{\left(\frac{s\pi}{l}\right)^2 + \left(\frac{\xi_{nm}}{a}\right)^2} \tag{3.1}$$

Where ξ_{nm} is the m^{th} root of the Bessel's function of n order, s=0,1,2,3... defining the mode variation law along the z-direction like: $\sin \frac{s\pi}{l} z$ (the s parameter represents also the number of the half wave lengths along z).

For the TE modes (3.2):

$$f_{res} = \frac{1}{2\pi\sqrt{\mu\varepsilon}} \cdot \sqrt{\left(\frac{s\pi}{l}\right)^2 + \left(\frac{\xi'_{nm}}{a}\right)^2} \tag{3.2}$$

Where ξ'_{nm} is the m^{th} root of the Bessel's derived function of n order, s=1,2,3...and defining the mode variation law along the z-direction like: $\sin \frac{s\pi}{l} \cdot z$ (the s parameter represents also the number of the half wave lengths along z).

3.2 Data obtained from CST Eigenmode simulations

The cavity structures with all the resonance frequencies were studied. These frequencies are a problem for the stability of the beam, because in correspondence of these modes there are peaks of impedance (it is a quantity that talks about the losses due to different coupling between the beam and the environment). Using the Eigenmode solver it is possible to determine the resonant modes and their kind, TM or TE, in more complicate structures than cylindrical cavity. During the simulations of this component, we didn't use the suggestion to reduce the number of mesh cells (with symmetry planes) given by the Riminucci's thesis [3], because the interconnect's structure didn't have symmetries at his boundaries. In the case symmetry planes were used, some frequencies, caused by the transverse impedances, would not be visible. For this reason were done three different, long and complete, simulations:

- The first, and several time cited, is the cylindrical cavity. Figure 3.2

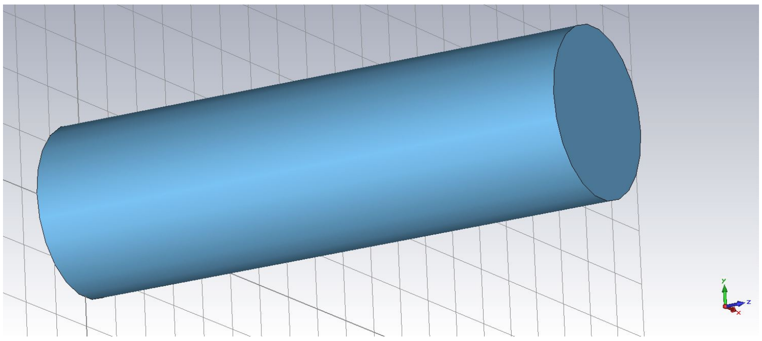

Figure 3.2. Cylindrical cavity

- The next analysis just for the interconnect cavity has been carried out Figure 3.3:

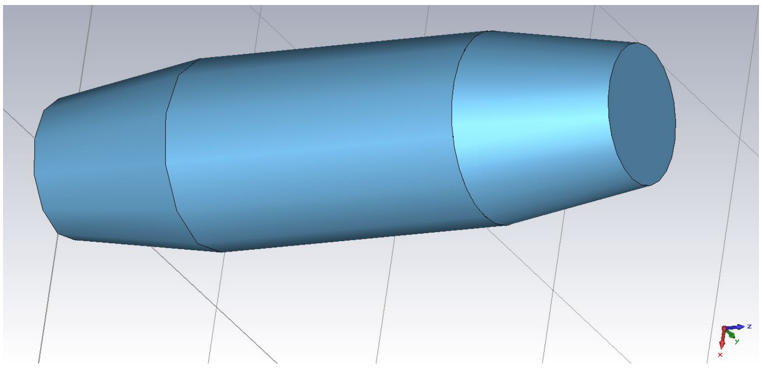

Figure 3.3. Cavity alone

- The whole component for the last simulation Figure 3.4:

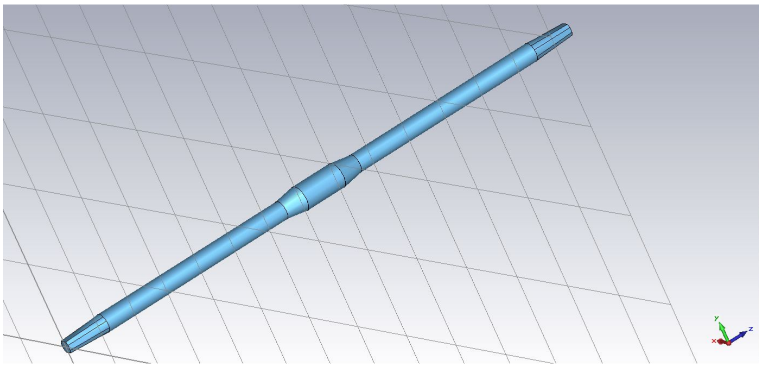

Figure 3.4. FCC interconnect between two magnets

3.2.1 Checked approximations and reality

In the following table Figure 3.5 different results are shown from left to right:

- Equations (Equation 3.1, Equation 3.2) have been solved thanks to a special Fortran 95 script.
- CST simulations of the cylindrical cavity for a first check between the CST eigenmode solutions and analytic equations.
- CST simulation just examinating the cavity of the component.
- CST simulation of the whole component.

Modes	Calculated	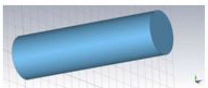	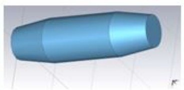	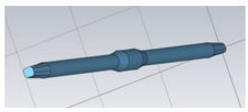
TE_{111}	3.022 [GHz]	3.023 [GHz]	3.064 [GHz]	3.058 [GHz]
TE_{112}	3.289 [GHz]	3.290 [GHz]	3.411 [GHz]	3.379 [GHz]
TE_{113}	3.692 [GHz]	3.692 [GHz]	3.864 [GHz]	3.746 [GHz]
TM_{010}	3.825 [GHz]	3.825 [GHz]	3.917 [GHz]	3.918 [GHz]
TM_{011}	3.898 [GHz]	3.898 [GHz]	4.180 [GHz]	-
TM_{012}	4.108 [GHz]	4.108 [GHz]	-	-
TE_{114}	4.190 [GHz]	4.191 [GHz]	4.365 [GHz]	-

Figure 3.5. Table of resonance frequencies

It has to be noticed that in the whole component after the first mode TM which is the TM_{010}, there isn't the TM_{011} as in the other three cases, but from the simulations it could be understood that the long parts of the interconnect started to resonate, these modes in the frequency step that go from the 3.995 GHz to 4.102 GHz are seven TE modes (example in Figure 3.6). Usually the most important mode is the first, that will be the limit for the excited EM fields in the standard working conditions of the particle accelerators.

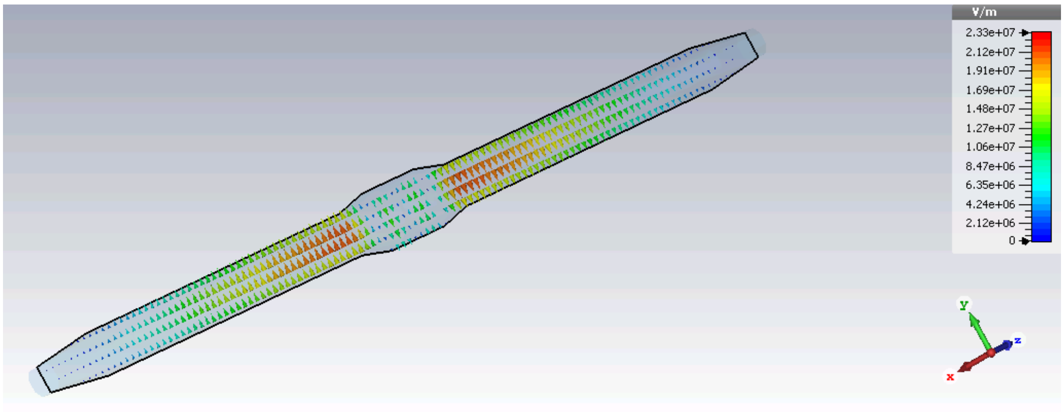

Figure 3.6. Whole component in resonance

3.3 First mode

Looking at the table in the precedent section that contains analytic calculation and simulations, it provides the first resonator mode in the component that is TE_{111}. The last check is an graphic method called "the mode chart" Figure 3.7, a map based on the analytic formula shown before "(3.1), (3.2)" concerning the cylindrical cavity.

Where the x axis and the y axis are described from the next formula. The real point over mode chart is given by the cylindrical cavity solution, even the point derived from the approximation using the first resonance frequency of the interconnect between two magnets is almost the same.

- For the cylindrical cavity:

$$\left(\frac{a}{l}\right)^2 = 0.0225 \tag{3.3}$$

$$\omega_0 = 2\pi f = 18,994\ GHz \tag{3.4}$$

$$\left(\frac{\omega_0 \cdot a}{c}\right)^2 = 3,61 \tag{3.5}$$

- For the approximation of the total element at a cylindrical cavity:

$$\left(\frac{a}{l}\right)^2 = 0.0225 \tag{3.6}$$

$$\omega_0 = 2\pi f = 19,214\ GHz \tag{3.7}$$

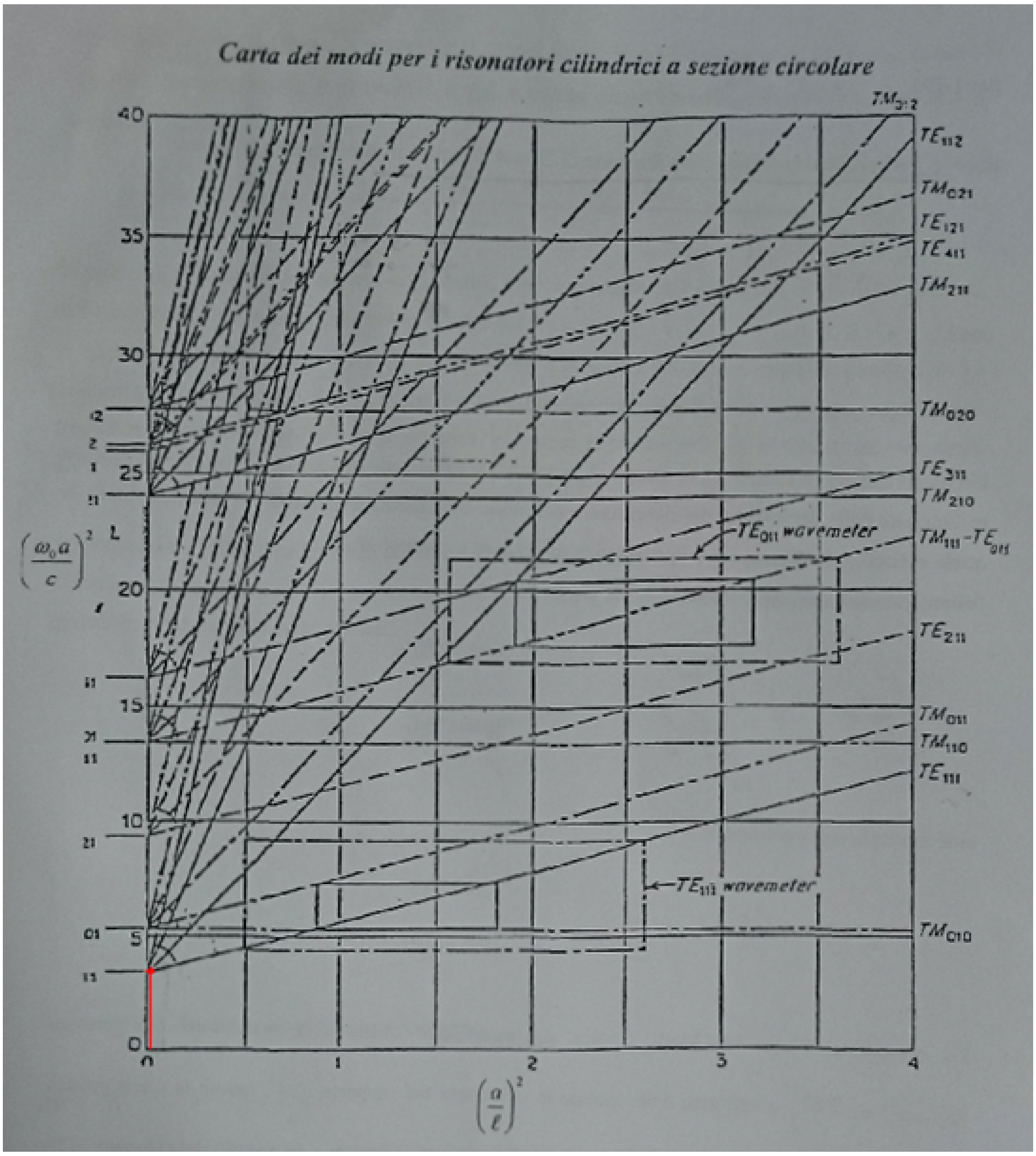

Figure 3.7. Mode chart

$$\left(\frac{\omega_0 \cdot a}{c}\right)^2 = 3,69 \tag{3.8}$$

TE_{111} is the mode verified also by the graphic results of the simulations, the Electric field for the first mode in 3D graphic for all simulations was shown below. Was even showed the magnetic field for the first mode in the whole interconnect.

Electric field of the three eigenmode simulations: Figure 3.8, Figure 3.9, Figure 3.10 and Figure 3.11

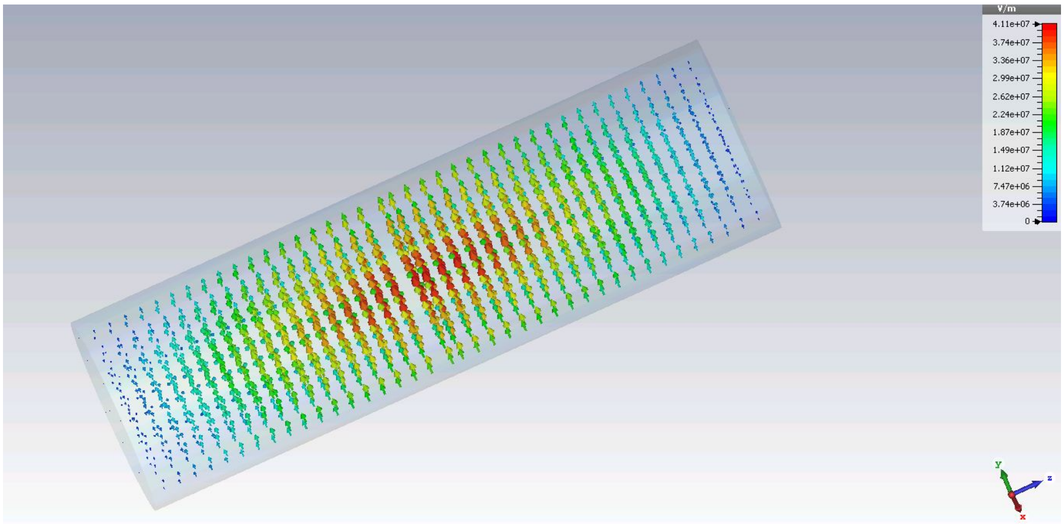

Figure 3.8. Electric field cylindrical cavity

Magnetic field only of the last and most important simulations: Figure 3.12, Figure 3.13

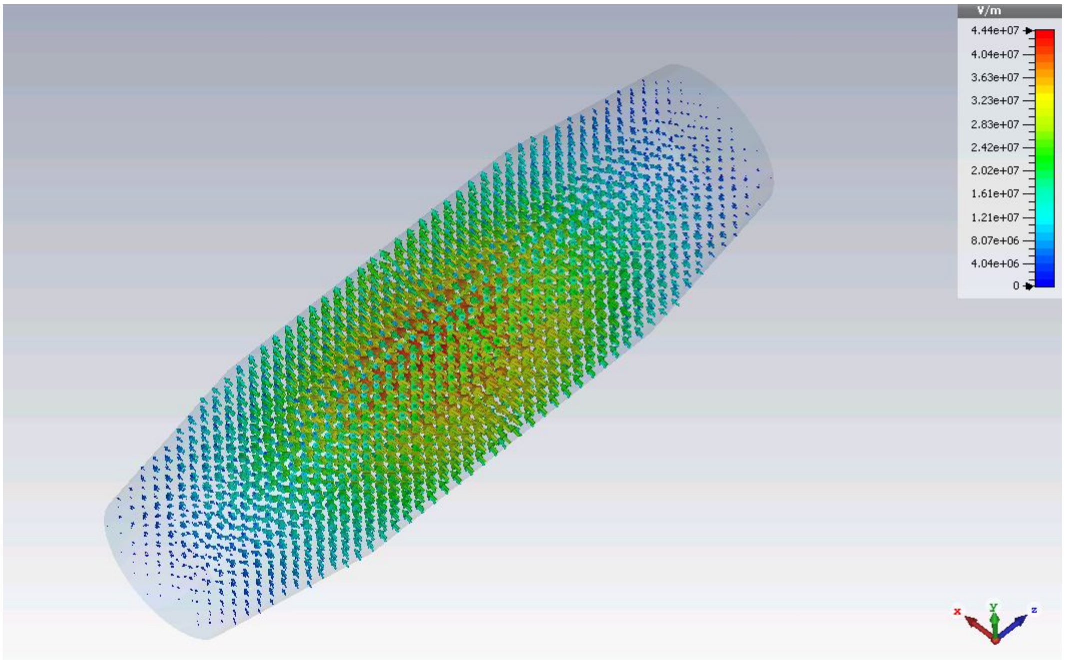

Figure 3.9. Electric field cavity alone

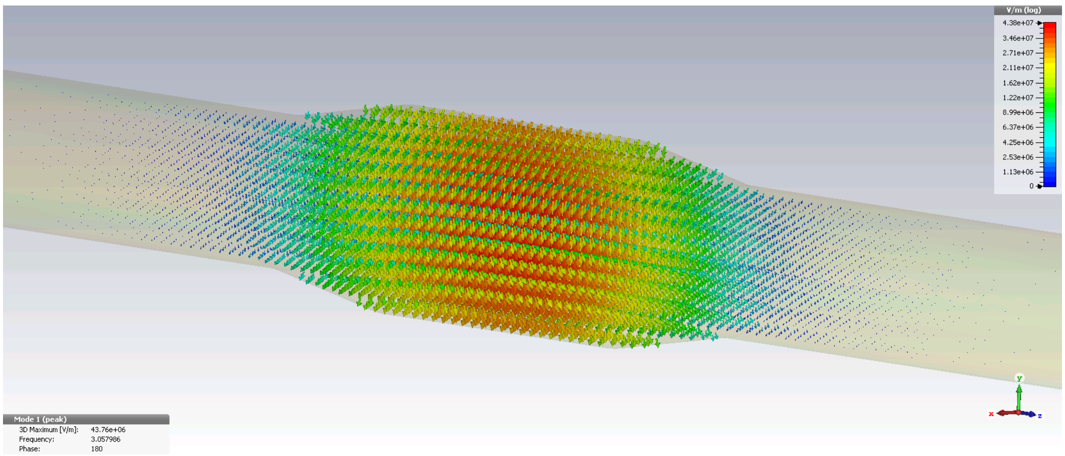

Figure 3.10. Electric field whole interconnect

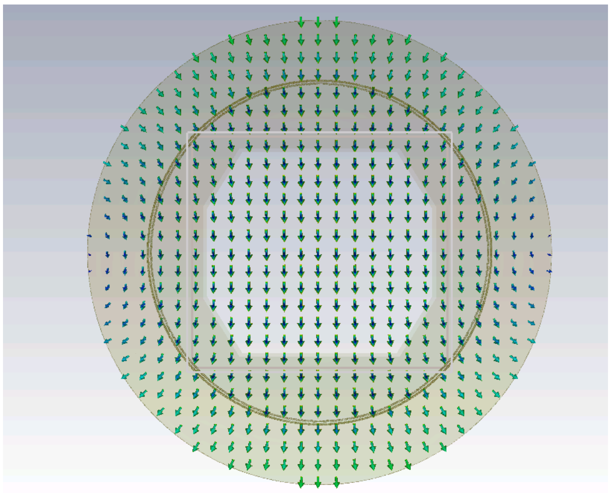

Figure 3.11. Electric field transverse cross section

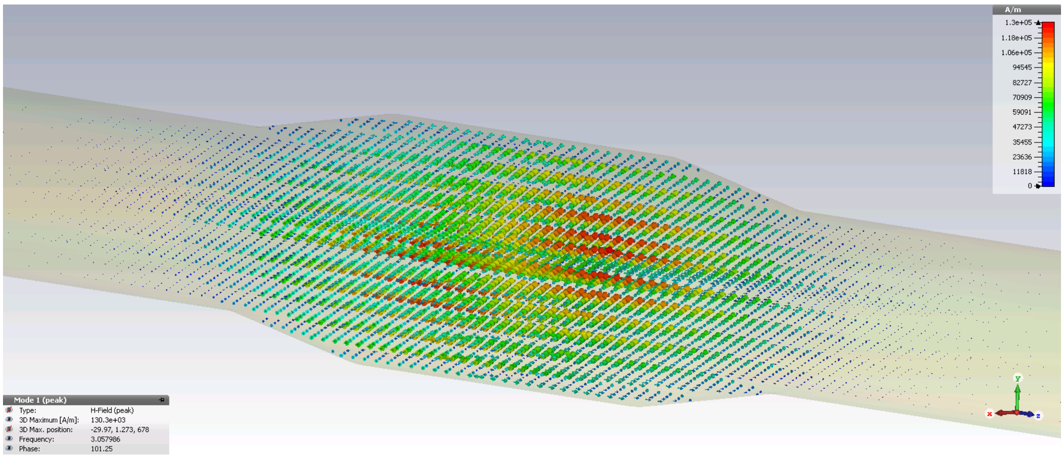

Figure 3.12. Magnetic field whole interconnect

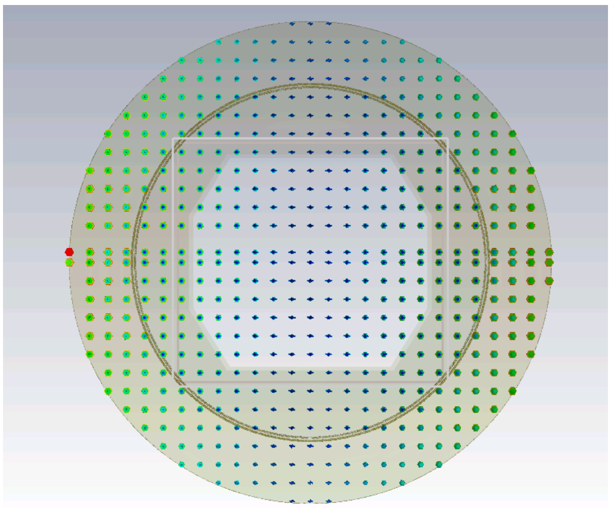

Figure 3.13. Magnetic field transverse cross section

Chapter 4

Wakefields and impedance theory

4.1 Wakefields

Wakefields [4] (in the context of accelerator physics) is the conventional name given when a charged particle called witness runs inside a beam pipe or a cavity where there is an EM field in the environment of this component excited from another charged particle called source that traversed the same structure before of it. Thus the "witness" particle is affected not only from its field but even from the field due by the "source" particle. Defined $r_1,\ q_1$ and $r_2,\ q_2$ the vectors position and charge of the first particle and the second particle respectively, where the space distance between the particles $r_1 - r_2$ was considered. The force on the second particle defined from Lorentz is (4.1):

$$F\left(r_1, r_2\right) = q_2[E + v \times B] \tag{4.1}$$

Where the longitudinal and transverse components were divided in (4.2) and (4.3):

$$F_{\parallel}\left(r_1, r_2\right) = q_2 E_{\parallel} \tag{4.2}$$

$$F_{\perp}\left(r_1, r_2\right) = q_2[E_{\perp} + (v \times B_{\perp})] \tag{4.3}$$

Where $E_{\parallel} = E_z\hat{z}$ and $E_{\perp} = E_x\hat{x} + E_y\hat{y}$. The studies of the impedance in these two components were divided.

4.1.1 Longitudinal wake function

Now providing the definition of the source particle energy (4.4):

$$U_1(r_1) = -\int_{-\infty}^{\infty} F_{\|}(r_1)dz \tag{4.4}$$

and the witness or second particle energy (4.5):

$$U_2(r_1, r_2, \tau) = -\int_{-\infty}^{\infty} F_{\|}(r_1, r_2)dz \tag{4.5}$$

Where the time $\tau = ((z_1 - z_2)/\beta c)$ and the force $F_{\|}(r_1, r_2) = q_2 E_{\|}(r_1, r_2)$. The longitudinal wake function for a charge particle is so defined (4.6):

$$w_{\|}(r_1, r_2, \tau) = \frac{U_2(r_1, r_2, \tau)}{q_1 q_2} \tag{4.6}$$

It is useful in the real case to define the wake function for a bunch distribution (4.9). Thus the charge q_1 as a integral of the current was defined (4.7):

$$q_1 = \int_{-\infty}^{\infty} i(\tau)d\tau \tag{4.7}$$

So that the energy for an infinitesimally $d\tau$ time was (4.8):

$$dU_2(r_2, \tau - \tau') = q_2 i(\tau') w_{\|}(r_2, \tau - \tau') \tag{4.8}$$

The longitudinal wake function for a bunch was defined below (4.9):

$$W_{\|}(r_2, \tau) = \frac{U(r_2, \tau)}{q_1 q_2} = \frac{1}{q_1} \int_{-\infty}^{\infty} i(\tau') w_{\|}(r_2, \tau - \tau') d\tau' \tag{4.9}$$

4.1.2 Transverse wake function

The same passage is valid also for transverse directions. The energy of the witness particle (4.10):

$$P(r_1, r_2, \tau) = \int_{-\infty}^{\infty} F_{\perp}(r_1, r_2)dz \tag{4.10}$$

Where the time $\tau = (z_1 - z_2/\beta c)$ and the force $F_{\perp}\,(r_1, r_2) = q_2[E_{\perp} + (v \times B_{\perp})]$. In this way is defined the transverse wake function for a charge particle (4.11):

$$w_{\perp}(r_1, r_2, \tau) = \frac{P(r_1, r_2, \tau)}{q_1 q_2} \tag{4.11}$$

Even in this real case is useful to define the wake function for a bunch distribution (4.14). Thus the charge q_1 as a integral of the current is defined (4.12):

$$q_1 = \int_{-\infty}^{\infty} i(\tau) d\tau \tag{4.12}$$

So that the energy for an infinitesimally $d\tau$ time is (4.13):

$$dP(r_2, \tau - \tau') = q_2 i(\tau') w_{\perp}(r_2, \tau - \tau') \tag{4.13}$$

The transverse wake function for a bunch is defined below:

$$W_{\perp}(r_2, \tau) = \frac{P(r_2, \tau)}{q_1 q_2} = \frac{1}{q_1} \int_{-\infty}^{\infty} i(\tau') w_{\perp}(r_2, \tau - \tau') d\tau' \tag{4.14}$$

4.2 Coupling impedance

Finally the coupling impedance for the different directions is so defined (4.15) and (4.16):

$$Z_{\parallel}(r_1, r_2, \omega) = \int_{-\infty}^{\infty} w_{\parallel}(r_1, r_2, \tau) e^{-j\omega\tau} d\tau \tag{4.15}$$

$$Z_{\perp}(r_1, r_2, \omega) = j \int_{-\infty}^{\infty} w_{\perp}(r_1, r_2, \tau) e^{-j\omega\tau} d\tau \tag{4.16}$$

Reversely, the wake function from the coupling impedance can be expressed like (4.17) and (4.18):

$$w_{\parallel}(r_1, r_2, \tau) = \frac{1}{2\pi} \int_{-\infty}^{\infty} Z_{\parallel}(r_1, r_2, \omega) e^{j\omega\tau}\, d\omega \tag{4.17}$$

$$w_{\perp}(r_1, r_2, \tau) = \frac{j}{2\pi} \int_{-\infty}^{\infty} Z_{\perp}(r_1, r_2, \omega) e^{j\omega\tau}\, d\omega \tag{4.18}$$

Often the wake function was treated in the time domain considering the current's distribution of the bunch that has to be considered in the Fourier's domain (4.19), usually the bunch current had a Gaussian shape. In this particular case it is the Wake Potential (4.20) and (4.21).

$$\lambda(\omega) = \int_{-\infty}^{\infty} i(\tau) e^{-j\omega\tau} d\tau \tag{4.19}$$

$$W_{\parallel}(r_2, \tau) = \frac{1}{2\pi} \int_{-\infty}^{\infty} Z_{\parallel}(r_1, r_2, \omega) \lambda(\omega) e^{j\omega\tau} d\omega \tag{4.20}$$

$$W_{\perp}(r_2, \tau) = \frac{j}{2\pi} \int_{-\infty}^{\infty} Z_{\perp}(r_1, r_2, \omega) \lambda(\omega) e^{j\omega\tau} d\omega \tag{4.21}$$

4.3 Transverse impedance

The transverse impedance depends on the bunch displacement. In particular how shown before two particular particles were studied: the source and witness particle. In the CST simulations the source particle is the blue beam that excite the EM fields and the witness is the orange integrator beam. It is useful to talk about of transverse impedance as composed from three different components. The first is called dipolar or driving impedance and will be obtained with a transverse source particle displacement, along x or y, leaving the witness particle centred. By definition, in this case, the witness particle “feels” a transverse force independent by its position because it is fixed [5]. We will talk of quadrupolar or detuning impedance when the rules of the beams is change, by definition the witness particle “feels” a transverse force linearly proportional to its displacement. Together at these both principal components even a constant term caused by the asymmetric structures should be taken in account for the two different directions: (4.22) and (4.23). In particular in this study only the dipolar component was considerate and shown later.

$$Z_{\perp,x}(x_1, x_2, \omega) = Z_{dip,x}(\omega)x_1 + Z_{quad,x}(\omega)x_2 + Z_{const,x}(\omega) \tag{4.22}$$

$$Z_{\perp,y}(y_1, y_2, \omega) = Z_{dip,y}(\omega)y_1 + Z_{quad,y}(\omega)y_2 + Z_{const,y}(\omega) \tag{4.23}$$

The procedure used in the CST simulations for the calculation of the dipolar component is easy shown in the picture below Figure 4.1 :

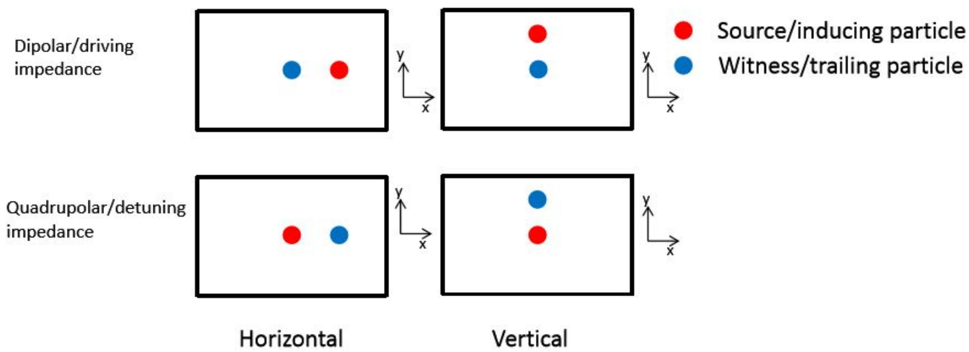

Figure 4.1. Different displacements for the dipolar or quadrupolar impedance

How said before the work is focused on the dipolar component.

Chapter 5

Wakefield CST simulation and relative impedance study

Trough the CST simulation in Wakefield mode, the values of the longitudinal and transverse impedance was found. The impedance was studied simulating inside the component of centred beams with respect to the transverse cross section of the own component. The view respect to the yz plane Figure 5.1.

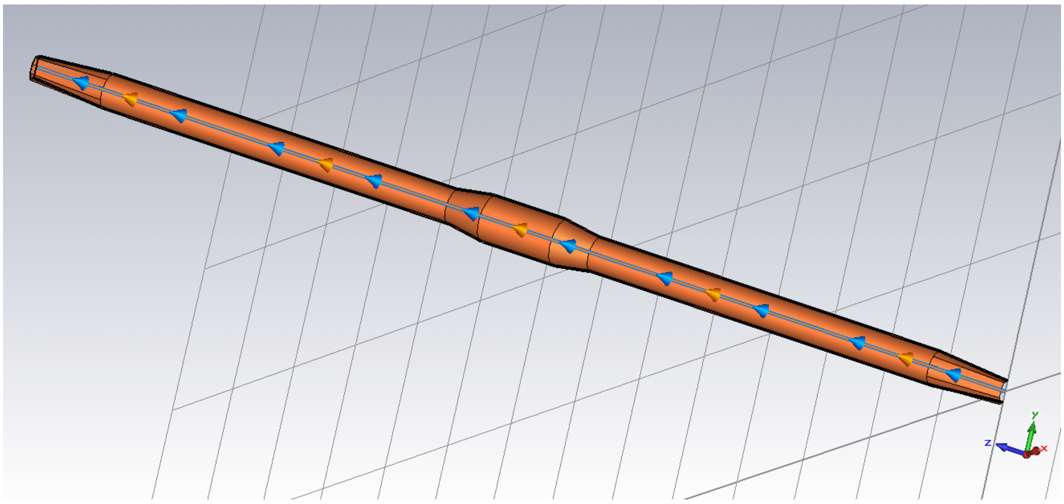

Figure 5.1. Component with centred beams

5.1 Longitudinal impedance: charts

The charts supplied by the simulations, starting from the wake potential and successively the own Fourier's transformer "the impedance", separated in the real and imaginary part will be shown below. The imaginary part of the longitudinal impedance, after being normalized with reference reference to frequency, can be used within Sacherer's formalism [6] to deduce the longitudinal beam stability.

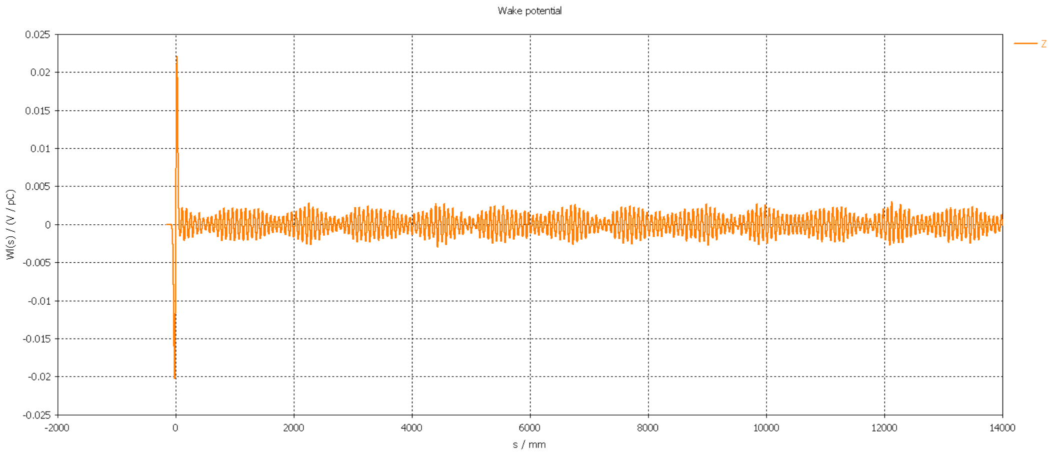

Figure 5.2. Wake potential calculated along the beam direction

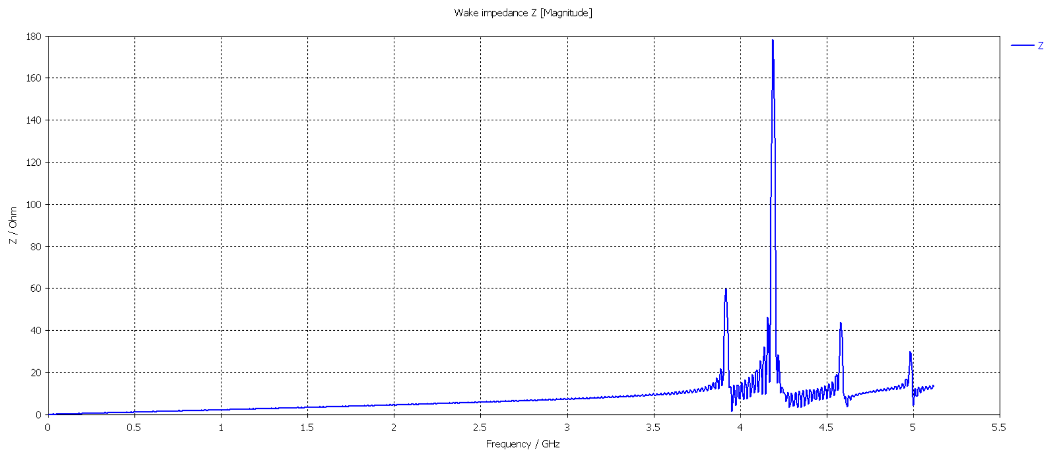

Figure 5.3. Whole longitudinal impedance

In particular the value of our interest was shown below, i.e. part of the angular coefficient of the linear imaginary part trend Figure 5.5 in the step of frequencies from the lowest value of the frequency (5.2) "given from the skin depth (5.1)" and the limit provideed from the first resonance frequency deriving from the longitudinal impedance. This correction has been done multiplying the function $Im[Z \parallel_Z]$ for f_{rev}/f, checking so in the final chart an almost constant trend, due to the existent linear relation between the values of the x axis and y axis of the charts.

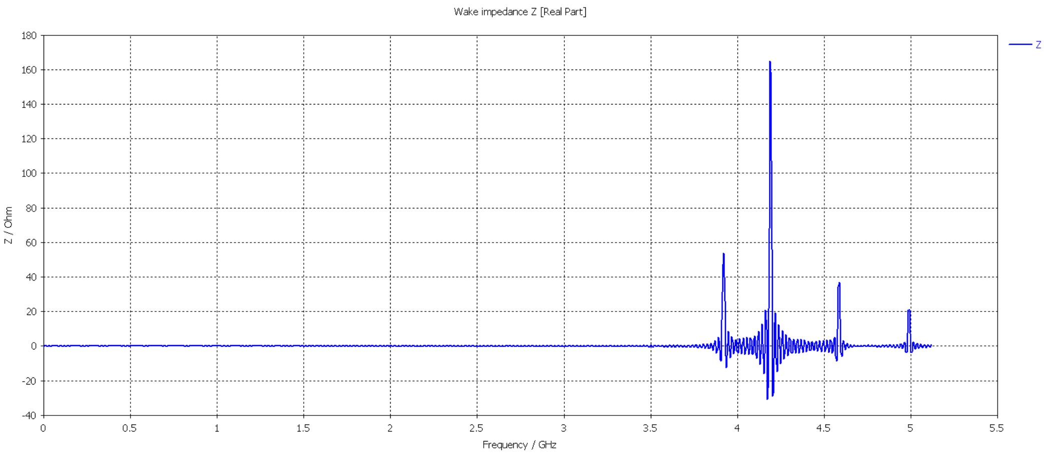

Figure 5.4. Longitudinal impedance: real part

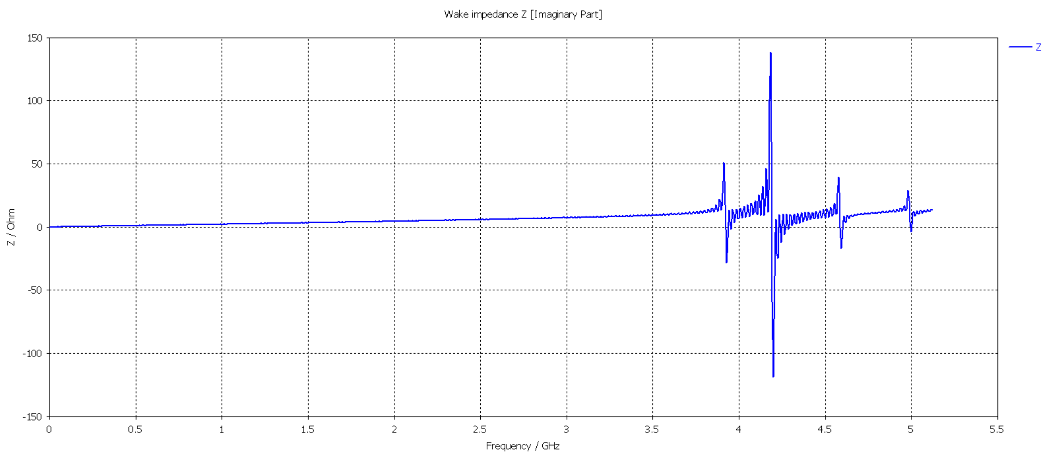

Figure 5.5. Longitudinal impedance: imaginary part

5.1.1 Skin depth

When the beam screen of the analysed component is made from a finite electric conductivity material, a very important parameter is the skin depth. It can be thought as the penetration distance of the magnetic field into the material [4], defined for high frequencies like :

$$\delta = \sqrt{\frac{2}{\omega \cdot \mu_0 \cdot \mu_r \cdot \sigma\,(50k)}} = 0.3 \cdot 10^{-3}\ mm \tag{5.1}$$

Where ω is the pulsation, μ_0 the permeability of the vacuum, μ_r the relative permeability of the material and $\sigma\,(50k)$ the electric conductivity of the beam screen. The value of the skin depth was supplied by the data sheet, in this case it is the thickness of the beam screen of interconnect it self, thanks to these data we are knowing that frequencies under the frequency f (5.2) will not be used to avoid issues like coupling between magnetic field and other lower conductivity materials.

$$f = \frac{1}{\pi \cdot \delta^2 \cdot \mu_0 \cdot \mu_r \cdot \sigma\,(50K)} = \frac{1}{(0,3 \cdot 10^{-3})^2 \cdot 4 \cdot \pi^2 \cdot 10^{-7} \cdot 1,33 \cdot 10^9} = 2,12\ kHz \tag{5.2}$$

5.1.2 Obtained results

The rectification was done to find the value $Im[Z\parallel_Z /n]$ where $n = f/f_{rev}^{FCC}$ and f_{rev}^{FCC} the revolution frequency of the particles bunch during the run in the FCC ring, this value is supplied from another resonance frequency which the LHC's f_{rev}^{LHC}, knowing that the beam will not be faster than the light speed cannot be reached in LHC.

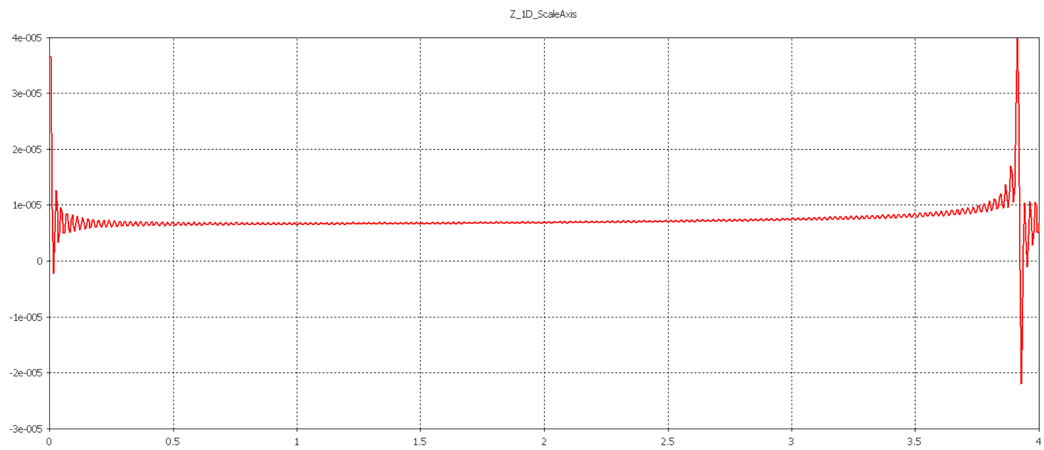

Figure 5.6. Longitudinal impedance in the broadband: rectified imaginary part

$$f_{rev}^{FCC} = \frac{f_{rev}^{LHC}}{3.70} = 3040\ Hz \tag{5.3}$$

Where $f_{rev}^{LHC} = 11245\ [Hz]$.

$$3,70 = \frac{length(FCC)}{length(LHC)} = \frac{100\ km}{27\ km} \tag{5.4}$$

From the chart the researched value was extracted:

$$Im\left[\frac{Z\parallel_z}{n}\right]_{tot} = 7e - 006 \cdot 4000 = 28\ m\Omega \tag{5.5}$$

Where 4000 is the total number of these components inside the whole FCC particles accelerator.

5.2 Transverse impedance

The dipolar transverse impedance is obtained during the simulation displacing the beam once along the x axis and in a different simulation displacing it along y axis, always leaving the integration beam at the centre. For the transverse impedance a work of convergence has been done: it has been checked the value of the broadband (the range from the lowest frequency to the frequency of the first resonant peak) increasing step by step the number of the mesh in the simulations (Figure 5.7, Figure 5.8) . In this mode most accurate value of the transverse impedance was found, with the lowest number of numerical errors due from the numerical CST computation. The problems of this check are the very long simulation times, it increases with the increasing of the mesh number.

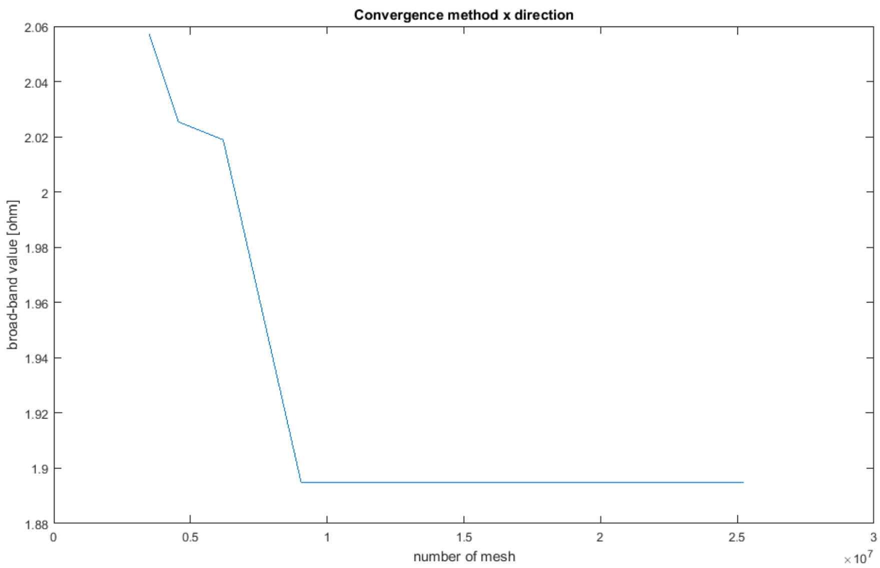

Figure 5.7. Mesh number convergence in beam position $(5, 0)\ mm$

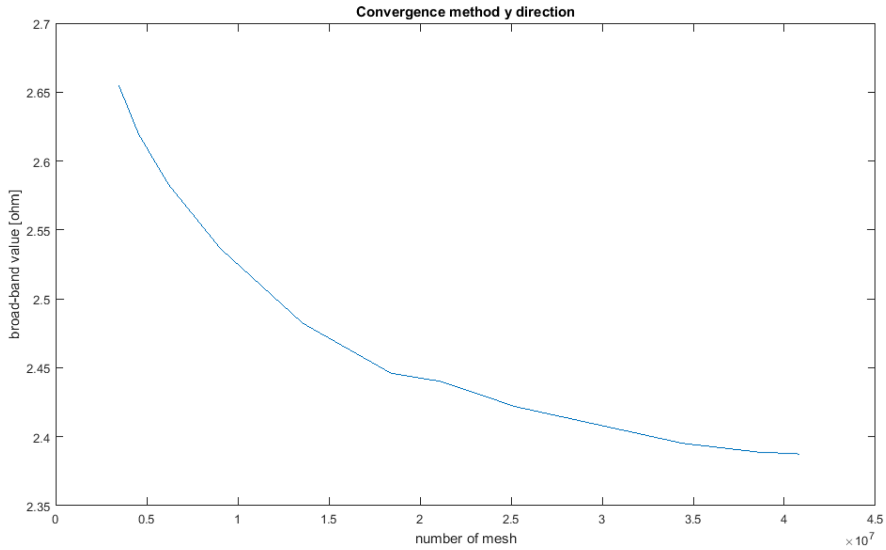

Figure 5.8. Mesh number convergence in beam position $(0, 5)$ mm

5.2.1 Transverse impedance x direction: position of the beam $(5, 0)$ mm in the plane xy

The title explain is shown in Figure 5.9:

Now all the charts related to the simulations, set off from the wake potential and next the Fourier's transformer of their "the impedance" divided even in real and imaginary component were shown below. The imaginary part of the transverse impedance can be used to compute the effective impedance in the plane of reference (x or y) in order to deduce the transverce beam stability within Sacherer's formalism [6].

5.2.2 Obtained results

The imaginary part of the transverse impedance in the area of interest, therefore under the first resonance frequency (the broad-band = $(Im[Z \perp_x] \cdot displacement)$) peak, due to the transverse impedance and not from longitudinal was found (5.6):

$$Im[Z \perp_x] \cdot displacement = 1,90\ \Omega \tag{5.6}$$

The value obtained from the chart will be divided for the transverse displacement because the transverse impedance is linearly dependent on it. In this case the displacement is 5 mm along x. Thus (5.7):

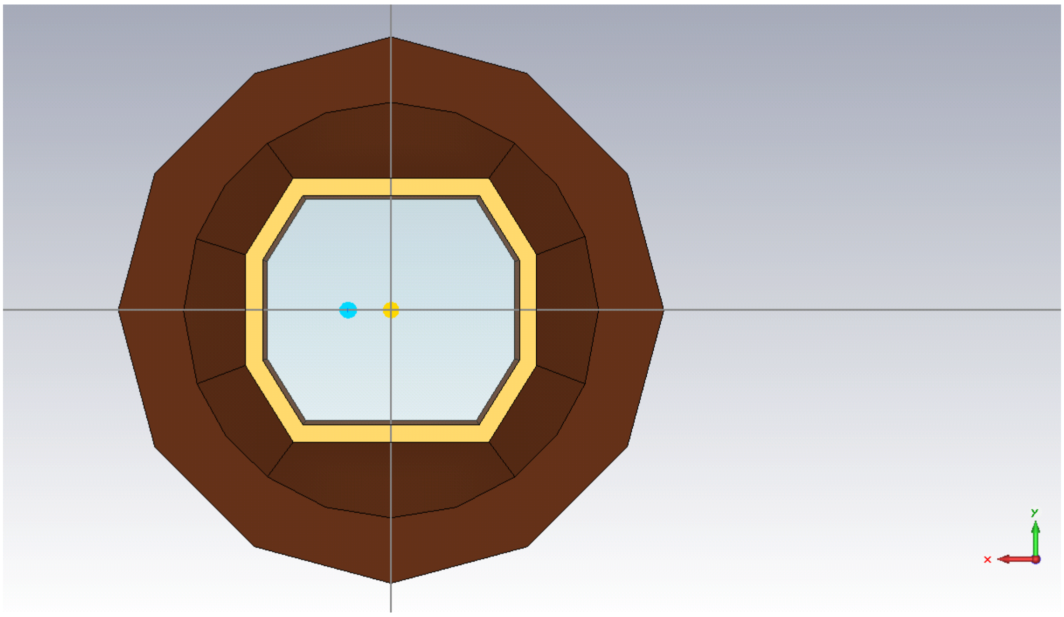

Figure 5.9. Interconnect with the beam in position $(5, 0)$ mm

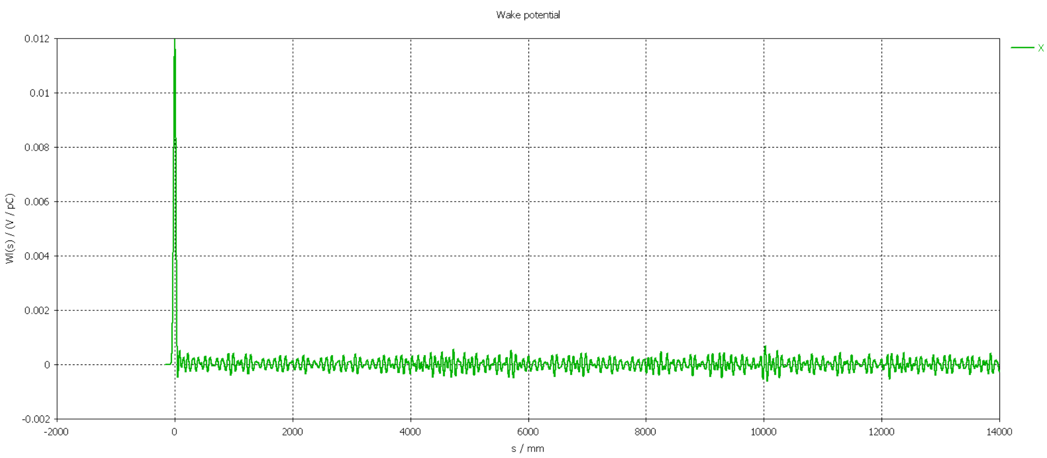

Figure 5.10. Wake potential calculated along the x direction

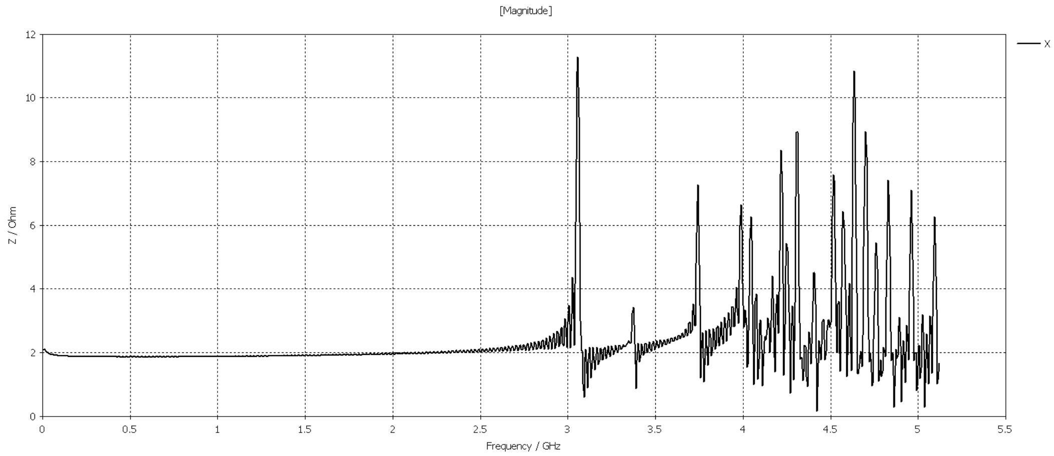

Figure 5.11. Whole transverse impedance x direction

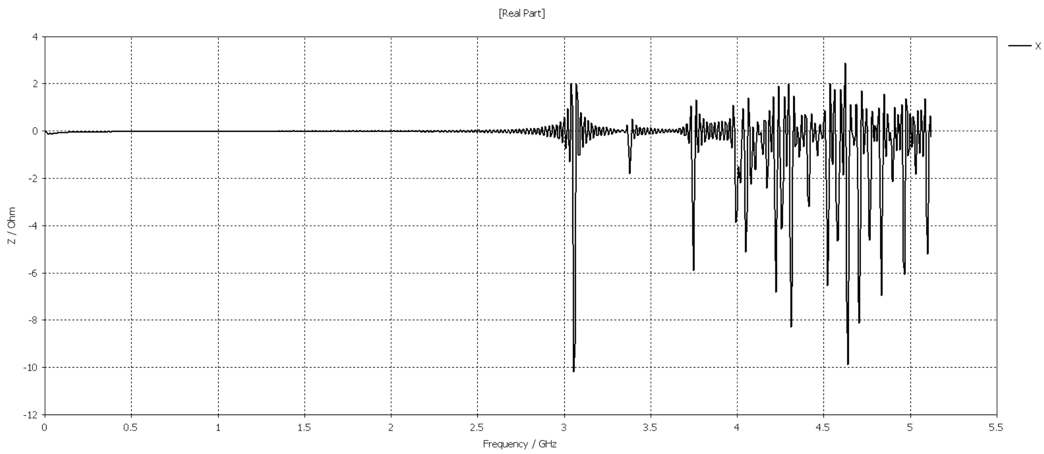

Figure 5.12. Transverse impedance x direction: real part

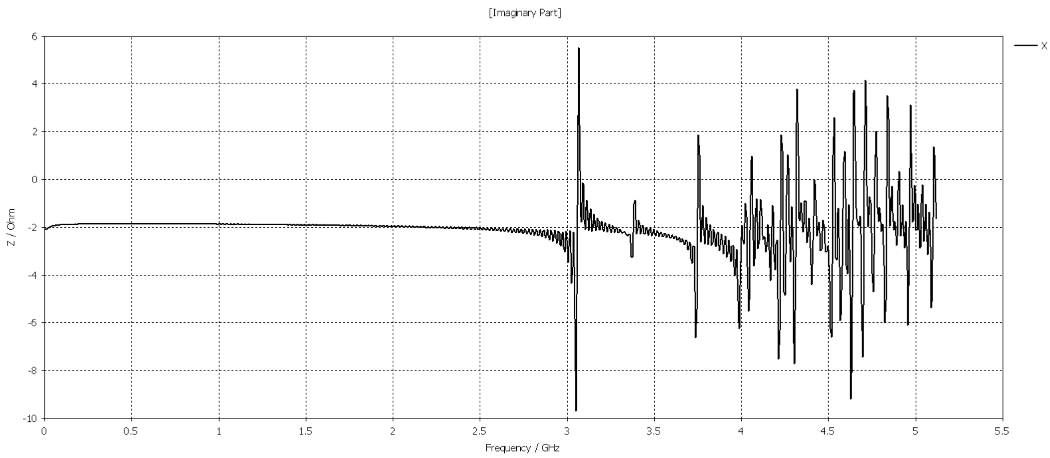

Figure 5.13. Transverse impedance x direction: imaginary part

$$Im[Z \perp_x] = 0,38\ k\Omega/m \tag{5.7}$$

To follow (5.8):

$$Im[Z \perp_x]_{tot} = 0,38 \cdot 4000 = 1,52\ M\Omega/m \tag{5.8}$$

Where 4000 is the total number of these components inside the whole FCC particles accelerator.

5.2.3 Transverse impedance y direction: position of the beam $(0,5)\ mm$ in the plane xy

The title explain is shown in Figure 5.14:

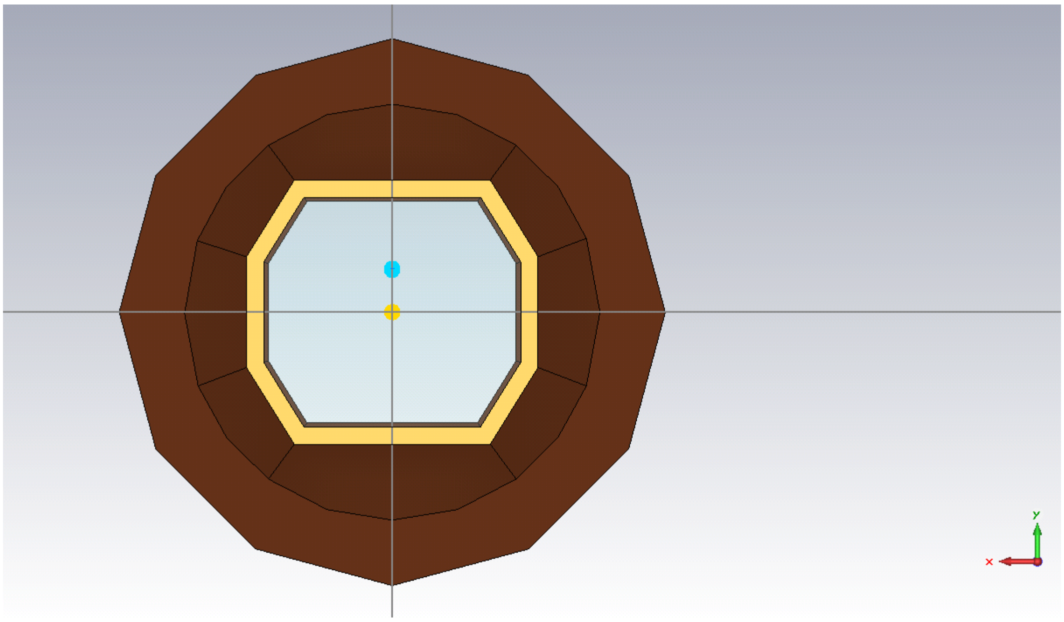

Figure 5.14. Interconnect with the beam in position $(0,5)\ mm$

5.2.4 Obtained results

The imaginary part of the transverse impedance in the area of our interest, therefore under the first resonance frequency (the broad-band = $(Im[Z \perp_y] \cdot displacement)$) peak, due to the transverse impedance and not from longitudinal was found (5.9):

$$Im[Z \perp_y] \cdot displacement = 2,4\ \Omega \tag{5.9}$$

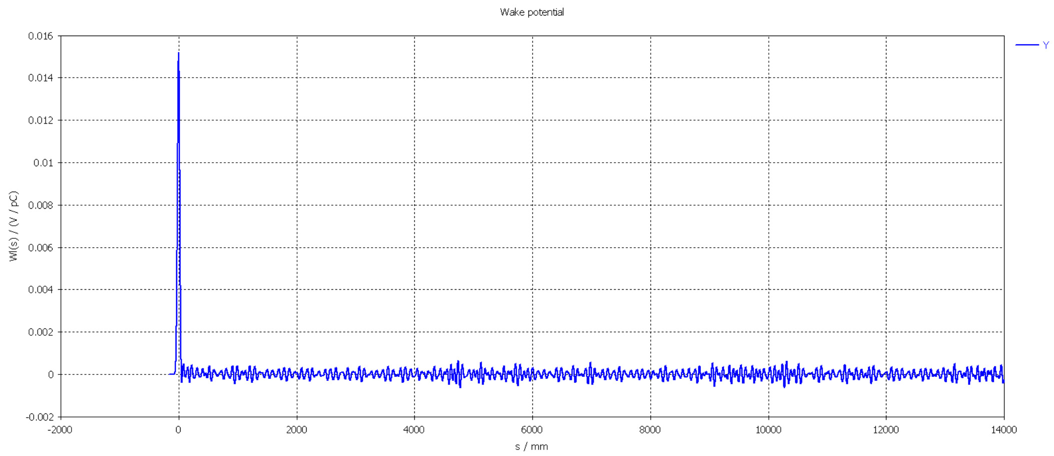

Figure 5.15. Wake potential calculated along the y direction

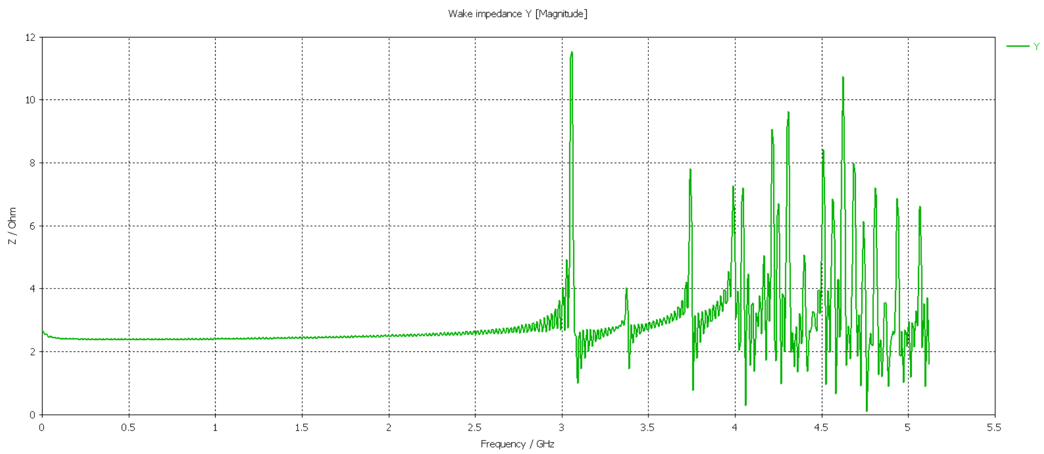

Figure 5.16. Whole transverse impedance y direction

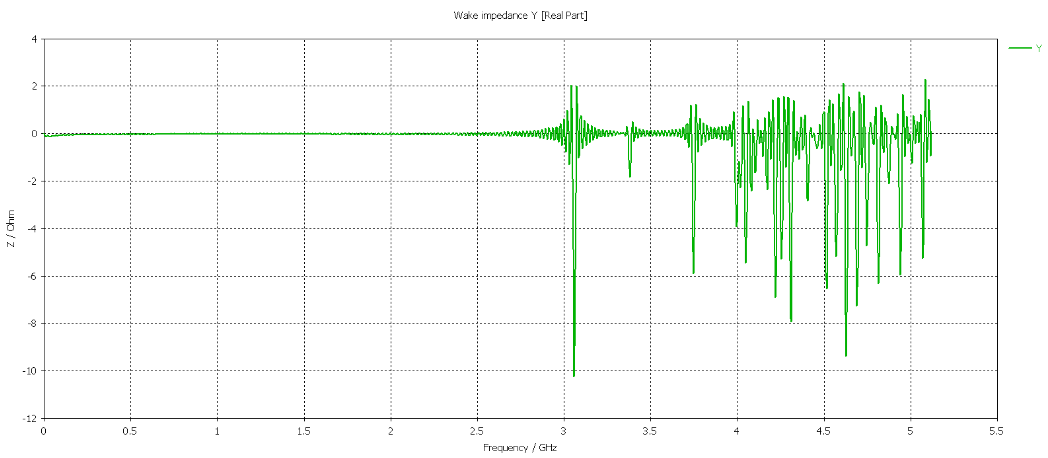

Figure 5.17. Transverse impedance y direction: real part

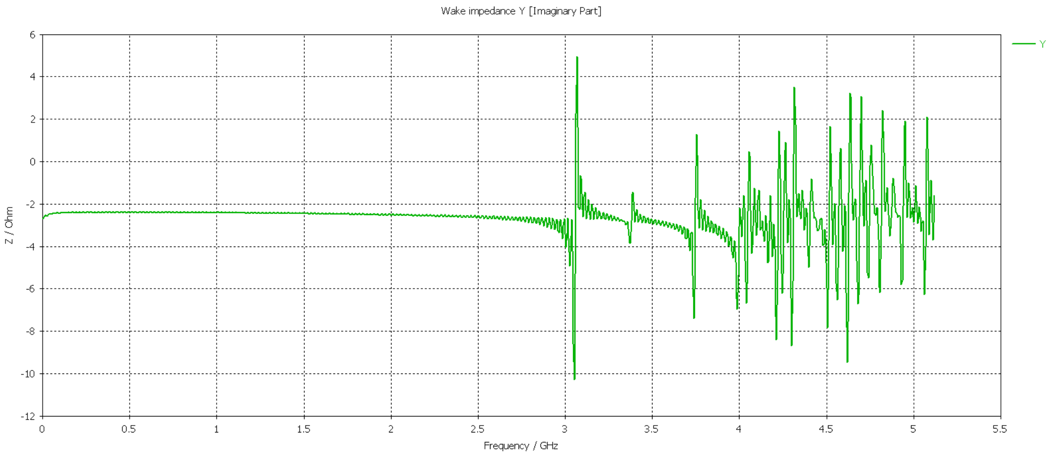

Figure 5.18. Transverse impedance y direction: imaginary part

The obtained value from the chart will be divided for the transverse displacement because the transverse impedance is linearly dependent on it. In our case the displacement is 5 mm along y. Thus (5.10):

$$Im[Z \perp_y] = 0,48\ k\Omega/m \tag{5.10}$$

To follow (5.11):

$$Im[Z \perp_y]_{tot} = 0,48 \cdot 4000 = 1,92\ M\Omega/m \tag{5.11}$$

Where 4000 is the total number of these components inside the whole FCC particles accelerator.

5.2.5 Conclusions

Found the values of the impedance, a check of the orders of magnitude between the impedance of the total number of interconnects in the FCC ((5.5),(5.8),(5.11)) and the same components in the LHC particle accelerator [7] has been done. Where the LHC data in the red rectangle was extracted Figure 5.19. Considering that the FCC will be four times longer than LHC, the longitudinal impedance (5.5) is almost three times larger than the same value in the LHC where we considered, for a comparison between the longitudinal impedances, the value n in LHC components must take in account the FCC revolution frequency. Also the transverse impedance ((5.8),(5.11)) are larger than the value in the last column multiplied for the FCC length $(0,265 \cdot 4 = 1,06M\Omega/m)$. From these previous observation we deduce that this first design of the interconnect isn't a good design. Instead for a first and simple impedance model of the whole FCC particle accelerator, thanks some impedance results about the components that are the largest in terms of impedance Figure 5.20 (the beam screen and collimators impedance model were made by David Amorim). The impact in the broad-band range gave by 4000 interconnects is negligible if we have considered the impact deriving from the sum between the beam screen and collimators impact. The graph show below is the imaginary part of the transverse impedance were in purple we see the interconnects transverse impedance in the worst condition. Therefore we could say that this first interconnect design considering only the broad-band is a good one.

element	Ref.	b	$\mathrm{Im}(Z/n)$	$\mathrm{Im}(Z_\perp)$
		mm	Ω	MΩ/m
Pumping slots	[23]	18	0.017	0.5
BPM's	[24]	25	0.0021	0.3
Unshielded bellows		25	0.0046	0.06
Shielded bellows		20	0.010	0.265
Vacuum valves		40	0.005	0.035
Experimental chambers		-	0.010	-
RF Cavities (400 MHz)		150	0.010	(0.011)
RF Cavities (200 MHz)		50	0.015	(0.155)
Y-chambers (8)	[25]	-	0.001	-
BI (non-BPM instruments)		40	0.001	0.012
space charge @injection	[2]	18	-0.006	0.02
Collimators @injection optics		$4.4 \div 8$	0.0005	0.15
Collimators @squeezed optics		$1.3 \div 3.8$	0.0005	1.5
TOTAL broad-band @injection optics			0.070	1.34
TOTAL broad-band @squeezed optics			0.076	2.67

Figure 5.19. Whole LHC impedance values in table

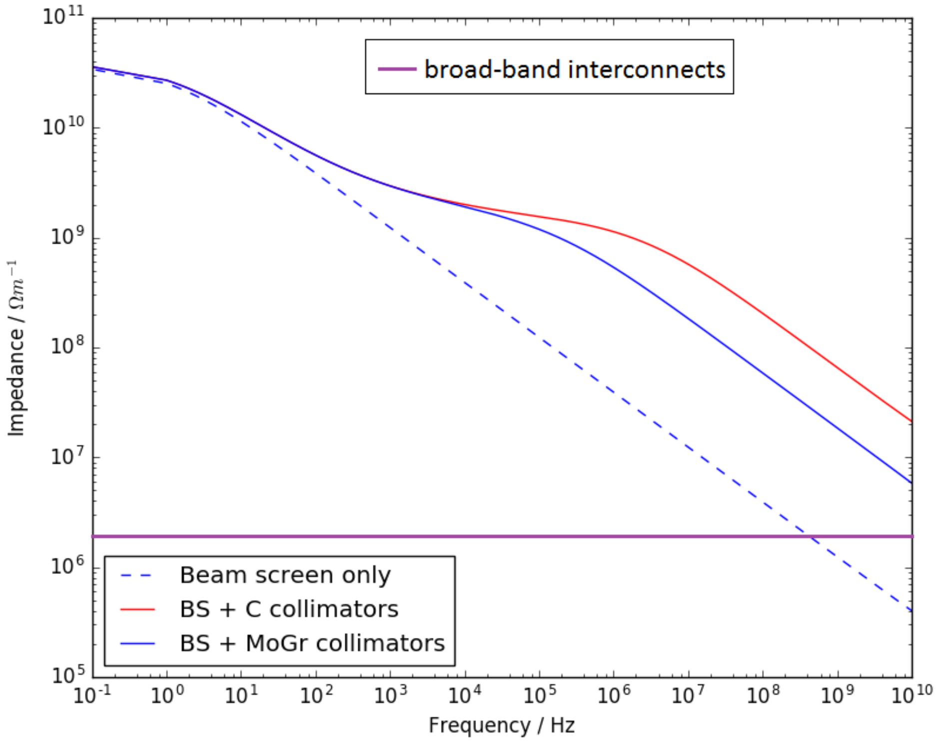

Figure 5.20. 1^{st} FCC impedance model: broad-band impact

Chapter 6

Shunt impedance

The resonator behaviour linked to the passive cavity is given by the big radius in the centre of the structure, after that another study over this interconnect has been done. Usually when there is a cavity and we want to analyse it in the frequency domain, the approximation like RLC load is the best thing. This equivalent circuit is driven from the i_b current and the loads are: the inductance L, the capacitance C and the shunt impedance Rs Figure 6.1:

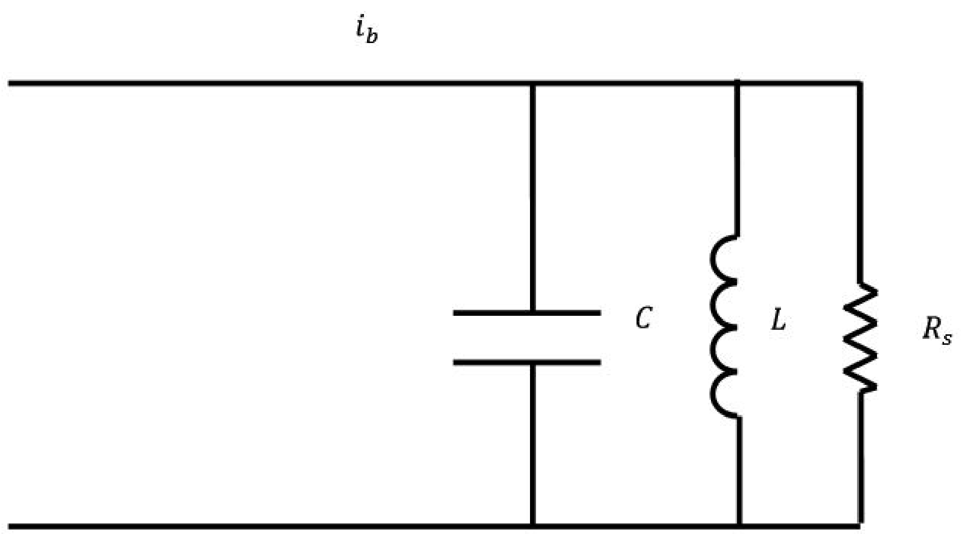

Figure 6.1. Equivalent circuit

The resonance frequency (6.1) also in a simple case like the cavity lossless where "$Rs = 0$ " [2] in this electric equivalent circuit is:

$$\omega_{res} = \frac{1}{\sqrt{LC}} \tag{6.1}$$

An important parameter for the real cavity, so with losses, is the quality factor [8] and it depends from mode and geometry. It describes the damping inside the cavity, to have a big $Q-factor$ is equal to have a long damping time. The $Q-factor$ is defined as ratio from powers stored upon missed (6.2):

$$Q = \omega_{res} \cdot \frac{energy\ stored\ in\ the\ cavity}{dissipated\ power\ over\ period} = \frac{\omega_{res} W}{P} \tag{6.2}$$

Where $W = \frac{C|V|^2}{2}$ and $P = \frac{|V|^2}{2R_s}$ and trough the appropriate substitutions provide this other relation (6.3):

$$Q = R_s \sqrt{\frac{C}{L}}. \tag{6.3}$$

Now the characteristic impedance is defined (6.4):

$$X = \sqrt{\frac{L}{C}} \tag{6.4}$$

The definition of (6.1) supplies also $X = \omega_{res} L = \frac{1}{\omega_{res} C}$.
Now the Q-factor as $Q = \frac{R_s}{X}$ is described.
The longitudinal impedance as Fourier's transform of the wake function in z direction, described from an RLC circuit is shown (6.5):

$$Z_{\parallel}(\omega) = \frac{1}{\frac{1}{R_{s\parallel}} + j(\omega C - \frac{1}{\omega L})} \tag{6.5}$$

Multiplying the part $(\omega C - \frac{1}{\omega L})$ up for $X = \sqrt{\frac{L}{C}}$, down for $X = \frac{R_s}{Q}$ and thanks the (6.1) the impedance is thus read (6.6):

$$Z(\omega)_{\parallel} = \frac{R_{s\parallel}}{1 + jQ(\frac{f}{f_{res}} - \frac{f_{res}}{f})} \tag{6.6}$$

This relation is used if we are talking about longitudinal impedance, always in the electric equivalent circuit, the transverse shunt impedance was defined like (6.7) [9]. In correspondence of resonance frequencies, in both formulas, the value of the shunt impedance is the same as the value of the impedance, and this simple relation will be one of the main check in the next paragraph.

$$Z(\omega)_{\perp} = \frac{f_{res}}{f} \frac{R_{s\perp}}{1 + jQ(\frac{f}{f_{res}} - \frac{f_{res}}{f})} \tag{6.7}$$

6.1 Relation between longitudinal end transverse shunt impedance

In this section the relation between the longitudinal and transverse shunt impedance thanks a big cross check was found. In particular the tools available are the theory checked from the bases, the eigenmode simulations with the post processing command, the MatLab programming language end at the end the wakefield simulations.

6.1.1 Theory bases

The introduction of the chapter talks about the definition of quality factor like: $Q = \frac{\omega_{res}W}{P}$ where $P = \frac{|V|^2}{2R_s}$ that provide this relation (6.31)

$$\frac{R_s}{Q} = \frac{|V|^2}{2\omega_{res}W} \tag{6.8}$$

Where quality factor Q doesn't depend from the direction, if longitudinal or transverse, instead the voltage V thus the shunt impedance R_s depends from these different components. Like in the chapter "Wakefields and impedance theory" but now all in frequency domain an important formula for the study of the theory is the Lorentz's force defined like (6.9)

$$F = F_{||} + F_{\perp} = q_2[E + (v \times B)] \tag{6.9}$$

Where the longitudinal and transverse components were divided in (6.10) and (6.11):

$$F_{||} = q_2 E_{||} \Rightarrow F_z = q_2 E_z \tag{6.10}$$

$$F_{\perp} = q_2[E_{\perp} + (v \times B_{\perp})] \Rightarrow F_x = q_2[E_x + (c \times B_y)] \; or \; F_y = q_2[E_y + (c \times B_x)] \tag{6.11}$$

The longitudinal voltage shown before (6.31), in a finite component is defined [4] along the s (longitudinal beam direction) like (6.12) :

$$V_{||} = \int_{z_0}^{z_l} \frac{F_{||}}{q_2} \cdot e^{j\frac{\omega_{res}}{v} \cdot z} \, dz \tag{6.12}$$

In this case is (6.13):

$$V_z = \int_0^l \frac{F_z}{q_2} \cdot e^{j\frac{\omega_{res}}{c} \cdot z} \, dz = \int_0^l E_z \cdot e^{j\frac{\omega_{res}}{c} \cdot z} \, dz \tag{6.13}$$

The transverse voltage in a finite component is defined along the s (longitudinal beam direction) like (6.14):

$$V_{\perp} = \int_{z_0}^{z_l} \frac{F_{\perp}}{q_2} \cdot e^{j\frac{\omega_{res}}{v} \cdot z} \, dz \tag{6.14}$$

In this case are (6.15) and (6.16)

$$V_x = \int_0^l \frac{F_x}{q_2} \cdot e^{j\frac{\omega_{res}}{c} \cdot z} \, dz = \int_0^l [E_x + (c \times B_y)] \cdot e^{j\frac{\omega_{res}}{c} \cdot z} \, dz \tag{6.15}$$

or

$$V_y = \int_0^l \frac{F_y}{q_2} \cdot e^{j\frac{\omega_{res}}{c}\cdot z}\ dz = \int_0^l [E_y + (c \times B_x)] \cdot e^{j\frac{\omega_{res}}{c}\cdot z}\ dz \tag{6.16}$$

Another very important electromagnetic theorem is the Panofsky-Wenzel theorem [10] defined like (6.17):

$$-\frac{1}{v}\frac{\partial}{\partial \tau}\omega_\perp (r_1, r_2, \tau) = \nabla_\perp \omega_z (r_1, r_2, \tau) \tag{6.17}$$

The Fourier transform of (6.17) gives the dipole transverse impedance on terms of the longitudinal one (6.18):

$$Z_\perp(r_1, r_2, \omega) = \frac{c}{\omega_{res}}\ \nabla_\perp\ Z_\parallel(r_1, r_2, \omega) \tag{6.18}$$

Now the impedance definition as function of electromagnetic fields in frequency domain [5], in longitudinal (6.19) and transverse (6.20) case were shown below:

$$Z_\parallel = \frac{1}{q_1}\int_{z_0}^{z_l} E_z \cdot e^{j\frac{\omega_{res}}{c}\cdot z}\ dz \tag{6.19}$$

$$Z_\perp = -j\frac{1}{q_1}\int_{z_0}^{z_l} [E_\perp + (v \times B_\perp)] \cdot e^{j\frac{\omega_{res}}{v}\cdot z}\ dz \tag{6.20}$$

With opportune substitutions in the Panofsky-Wenzel theorem for the impedance (6.18), the relation with the electromagnetic fields was found (6.21):

$$-j\int_{z_0}^{z_l} [E_\perp + (v \times B_\perp)] \cdot e^{j\frac{\omega_{res}}{v}\cdot z}\ dz = \frac{c}{\omega_{res}}\ \nabla_\perp \int_{z_0}^{z_l} E_z \cdot e^{j\frac{\omega_{res}}{v}\cdot z}\ dz \tag{6.21}$$

Which thanks the definition of the voltage was wrote like (6.22):

$$-jV_\perp = \frac{c}{\omega_{res}}\ \nabla_\perp\ V_\parallel \tag{6.22}$$

In the "Wakefield CST simulation and relative impedance study" chapter, the study of the impedance was focused over the dipolar component of the transverse impedance. In the same mode the transverse shunt impedance due to the displacement of the beam, leaving the integrator beam at the centre, is divided in: transverse shunt impedance with x displacement and transverse shunt impedance with y displacement. The gradient $\nabla_\perp$ will be respectively $\frac{\partial}{\partial x}$ and $\frac{\partial}{\partial y}$. With the post processing results of the eigenmode simulation, for the FCC interconnect, the values of the E_z seen along the z direction were extracted like an ASCII data sheet. These trends of the electric field for different y displacement from $-15\ mm$ to $15\ mm$ has been calculated with several samples. A particular script MatLab has been made for found the trend of E_z respect the y displacement. Now using the voltage definition (6.23) the dependence with y didn't change.

$$V_z(y) = \int_0^l E_z(y) \cdot e^{j\frac{\omega_{res}}{c}\cdot z}\ dz = \int_0^l E_z(y) \cdot \left(\cos\left(\frac{\omega_{res}}{c}z\right) + j\sin\left(\frac{\omega_{res}}{c}z\right)\right)\ dz \tag{6.23}$$

Where $V_z(y) = V_{zreal}(y) + jV_{zimag}(y)$ and its absolute value in the script was found (6.24).

$$|V_z(y)| = \sqrt{V_{zreal}(y)^2 + V_{zimag}(y)^2} \tag{6.24}$$

From all these relation the law of dependence along y direction is constant for every displacements but not equal to the variation of y, if we bring out from the root this constant value it is in absolute value. Thanks to several wakefield mode simulations, in correspondence of the peaks (the shunt impedance) in the dipolar transverse impedance given from resonant frequencies and respective mode, the absolute value of the voltage change like $|y|$. The absolute value of the voltage for the second resonant mode of the interconnect is showed below Figure 6.2:

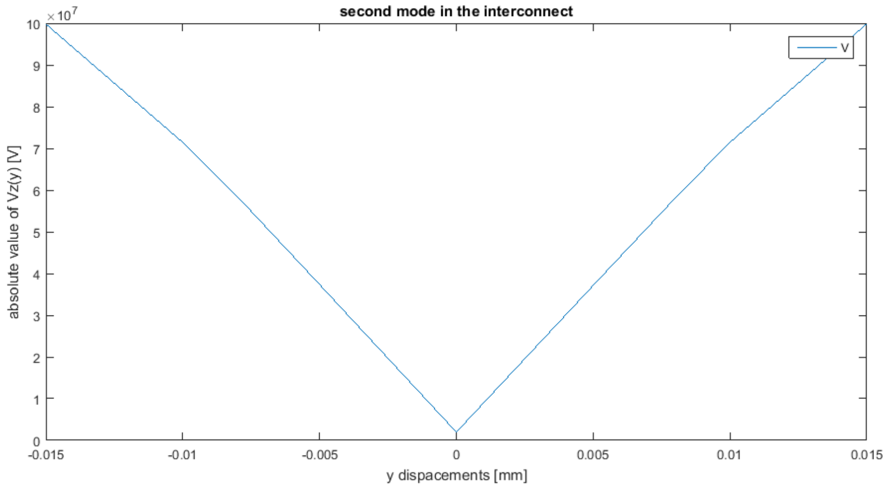

Figure 6.2. $|V_z(y)|$ trend

This check that when we have the transverse shunt impedance the $V_{\parallel}$ is linear dependent from the displacement y, it provides (6.25):

$$\nabla_{\perp} V_{\parallel} = \frac{\partial}{\partial y}\left[V_{\parallel}\right] = \frac{V_{\parallel}}{y} \tag{6.25}$$

From the (6.25) and (6.22) the linear relation between the longitudinal and transverse voltage, when there is the transverse shunt impedance, was found (6.26):

$$V_{\perp} = j\frac{c}{\omega_{res}}\frac{V_{\parallel}}{y} \Rightarrow |V_{\perp}|^2 = \left(\frac{c}{\omega_{res}} \cdot \frac{1}{y}\right)^2 \left|V_{\parallel}\right|^2 \tag{6.26}$$

Thanks to the definition of the ratio between the shunt impedance R_s and the quality factor Q wrote in (6.31) and the last formula (6.26), the relation between the different shunt impedance was found (6.27):

$$\frac{R_{s\perp}}{Q} = \frac{|V_{\perp}|^2}{2\omega_{res}W} = \left(\frac{c}{\omega_{res}} \cdot \frac{1}{y}\right)^2 \frac{\left|V_{\parallel}\right|^2}{2\omega_{res}W} = \left(\frac{c}{\omega_{res}} \cdot \frac{1}{y}\right)^2 \frac{R_{s\parallel}}{Q} \tag{6.27}$$

The final trend of the longitudinal shunt impedance for a specific mode is (6.28). It has a pure parabolic trend with the transverse displacement y where the transverse shunt impedance is part of the second order term [11]. In particular thanks to this experimental check, the fact that the transverse shunt impedance is independent from the transverse displacement, leads to the definition of dipolar modes given in the section "Transverse impedance"

$$R_{s\parallel} = R_{s\perp} \frac{\omega_{res}^2}{c^2} \cdot y^2 \; [\Omega] \tag{6.28}$$

The last formula for all cavities could be used and is equal for the x displacement, principally the mode TE where $E_{\parallel} = 0$ will not give transverse shunt impedance given by the Panofsky-Wenzel theorem (6.18), but in the real design of the component the transition between the cavity and the pipe will give a contribute of $E_{\parallel}$ and thus transverse shunt impedance. In particular we will see that the transverse shunt impedance depends even from the polarity of the resonant wave inside the structure, for example if the R_{sy} is searched when the polarity of the electric field is larger in the direction x than the direction y, we will have a little R_{sy} or zero. The maximum value of R_{sy} will be when the polarity of the wave is larger in the y direction.

6.2 Cross check

6.2.1 Wakefield, shunt impedance

How said during this chapter a large number of crosschecks between theory and CST simulations has been done. In particular for this work we didn't use the interconnect, but a pillbox cavity Figure 6.3 were the time of the simulation are faster because the shape is easier than the interconnect. This check is a perfect one because the theory is applicable always for every cavity. For the wakefield simulations and a quicker saturation of the peaks, has not been used the copper at 50 $[K]$ that has very few losses but another lossy metal with the electric conductivity $\sigma = 10^{-4}\ S \cdot m$. This material will bring at a faster convergence to zero of the wake potential Figure 6.4, because its damping is quicker than the wake potential Figure 5.15 dumping of very good conductive copper at $T = 50\ K$ that is almost a PEC material. The impedance Figure 6.5 is calculated as Fourier's transform of the wake potential in overall length interval (s). In CST simulations, the wake potential, before being transformed in the frequency domain, is multiplied by the wake lenght (wl) limited-length rect(s) function as defined in (6.29). The computation time increases as the wake length increases. If the wake potential decay to zero, the peaks of the resonances will be correctly saturated Figure 6.6. Conversely, a convergence study of the impedance as a function of the wake length will be necessary. In particular how said during the theory introduction, the mode that has given these peaks are the transition between cavity and the pipes Figure 6.7:

$$rect(s) = \begin{cases} 1 \;\; \forall \;\; -wl \leq s \leq +wl \\ 0 \;\; \forall \;\; s < -wl \;\; \vee \;\; s > +wl \end{cases} \tag{6.29}$$

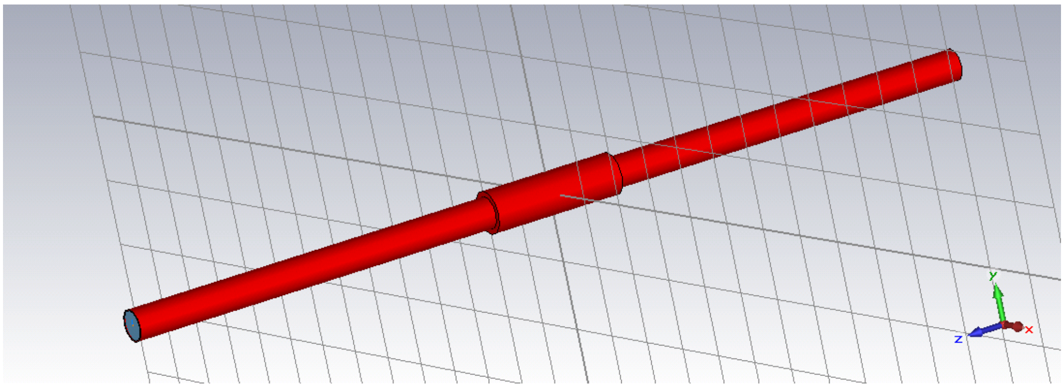

Figure 6.3. Pillbox cavity

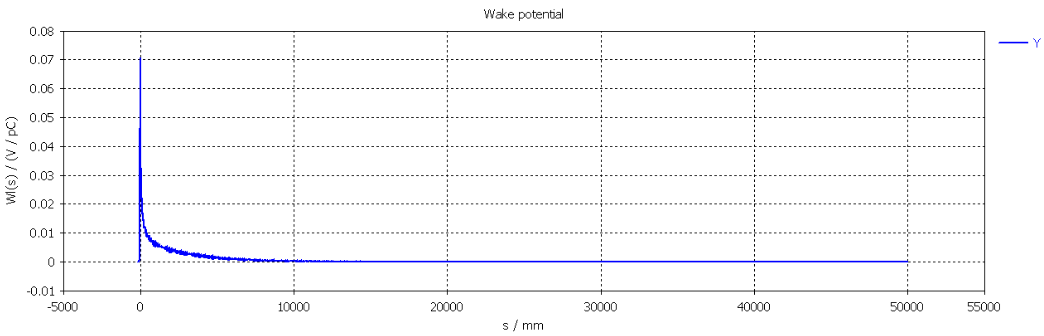

Figure 6.4. Transverse pillbox wakepotential y direction

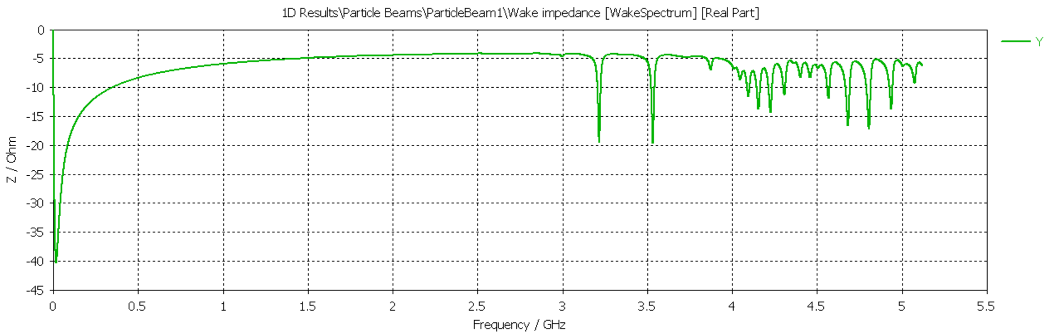

Figure 6.5. Transverse pillbox impedance y direction

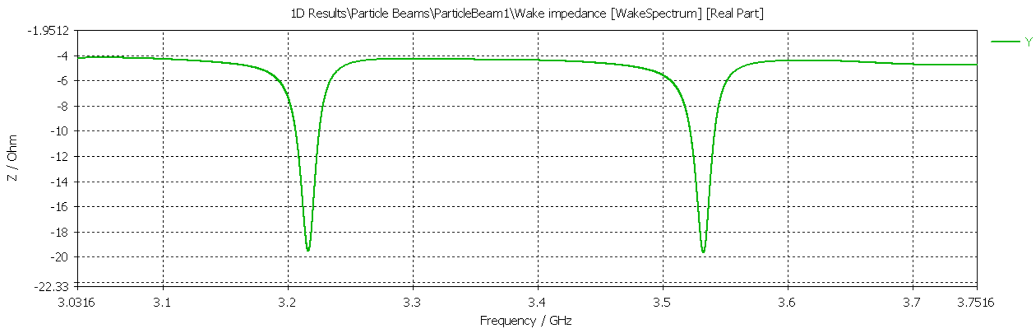

Figure 6.6. Peaks, transverse pillbox impedance y direction

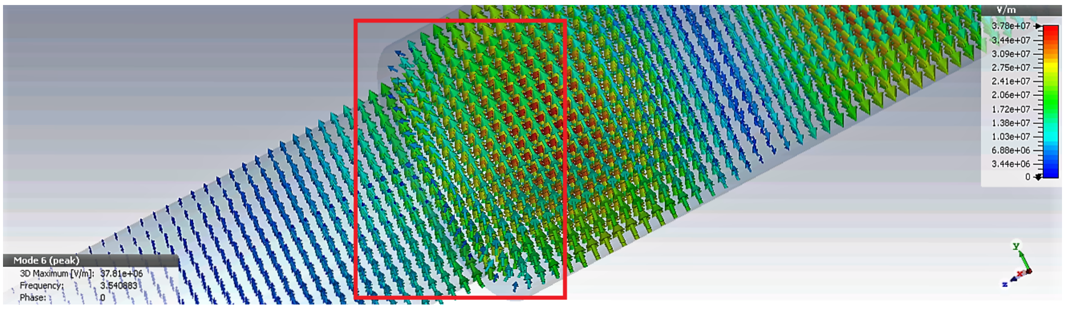

Figure 6.7. Pillbox transition of the electric field

Wakefield convention

How displayed in the "Transverse impedance" section the transverse impedance in the wakefield simulation vary linearly with the displacement and the peaks as well. Thus the value of the peaks Figure 6.6 (transverse shunt impedance), of different mode, will be divided for the displacement, that in this simulations is 5 mm.

The dimension of the shunt impedance will not be $[\Omega]$ as theory but $\left[\frac{\Omega}{m}\right]$ like the transverse impedance found before. The convention that give the relation between the theory transverse shunt impedance and the wakefield convention is (6.30):

$$R_{s\parallel} = R^W_{s\perp} \frac{\omega_{res}}{c} \cdot y^2 \tag{6.30}$$

Where the wake transverse shunt impedance $R^W_{s\perp} = R_{s\perp} \frac{\omega_{res}}{c} \left[\frac{\Omega}{m}\right]$.

6.2.2 Eigenmode, shunt impedance

An important command for the study of the shunt impedance, is the post processing. Thanks to it, it is possible to take from the CST simulation a lot of parameter for every mode, for example in these study: Q-factor, Frequencies, the longitudinal shunt impedance and values of Electric field and Magnetic field in all directions. All the parameters can be extract like ASCII file. Several checks for verify the theory with the eigenmode simulation have been done. With the help of several and specific scripts MatLab which reproduced the theory the longitudinal shunt impedance (6.31) where V is (6.12) and $R_s = R_{s\parallel}$ was found. Then after a first check with the longitudinal shunt impedance, given by the post processing command, the next step has been confirmed thanks to another script MatLab the last theory shunt impedance relation (6.28) with the theory definition of the transverse shunt impedance (6.31) where V is (6.14) and $R_s = R_{s\perp}$. In this check the displacement was fixed and the read files from the script were the Electric and Magnetic fields, the Q-factors and the Frequencies always for every mode. One of the most important checks before writing the last program, for the calculation of the transverse shunt, starting from the longitudinal shunt impedance given by the eigenmode simulation, has been varying the displacement along one of the transverse direction, fixed one mode, and calculated for each displacement longitudinal and transverse shunt impedance. The same script was used for several resonance frequencies relative or not to the peaks given in the wakefield simulation. It has been verified that for the frequencies in correspondence of the peaks (transverse shunt impedance) the values calculated from the script of the transverse shunt impedance are constant with the displacement, instead the longitudinal shunt impedance changed with the square of the displacement. All these checks confirmed the theory (6.28) and a more important result is that $R_{s\perp}$ is a constant part of the coefficient of the second order for each frequency connected with the transverse impedance peaks Figure 6.6.

Eigenmode convention

The eigenmode simulation for the calculation of the longitudinal shunt impedance use the definition shown in the theory (6.31) but without the factor 2. The transverse shunt impedance will be the same definition for the eigen convention.

$$R^E_s = Q \cdot \frac{V^2}{\omega_{res} W} \tag{6.31}$$

Where Q and V are dependent from the mode i.e. from ω_{res}, W is dependent from the structure and also from Q.

This convention was used for all scripts MatLab cited before. The last script as said before is used for the calculation of the transverse shunt impedance starting from the longitudinal shunt impedance given by the post processing. The particularity of the longitudinal shunt impedances in output from CST is that they varied with the resonance frequencies and with the displacement, so the script MatLab read the longitudinal shunt impedances calculated several times in the post processing, one time for each displacement (for example from $-10\ mm$ to $+10\ mm$ with several samples inside). After that the program do the best trend of the pure parabola linked to the variation of the longitudinal shunt impedance with the displacement for a fixed mode. In the case that this approximate trend is equal to the classic plot of the longitudinal shunt impedances read in order to the displacements, means that the theory relation (6.28) was verified. Now take the coefficient of second order that is the output of the parabola approximated, multiplying it for the value $\frac{c^2}{\omega_{res}{}^2}$ for each mode, the values of transverse shunt impedances $R^E_{s\perp}$ will be the output. These values in output are larger than the theoretical values of a factor 2 due to the eigen convention, therefor they are different for a factor $\frac{\omega_{res}}{2c}$ with the values of the wake convention.

Script-Eigenmode results

For the pillbox cavity with low electrical conductivity Figure 6.3, the results ($R^E_{s\perp}$), for only displacement along the y direction, given from the script MatLab that use the eigenmode convention are Figure 6.8:

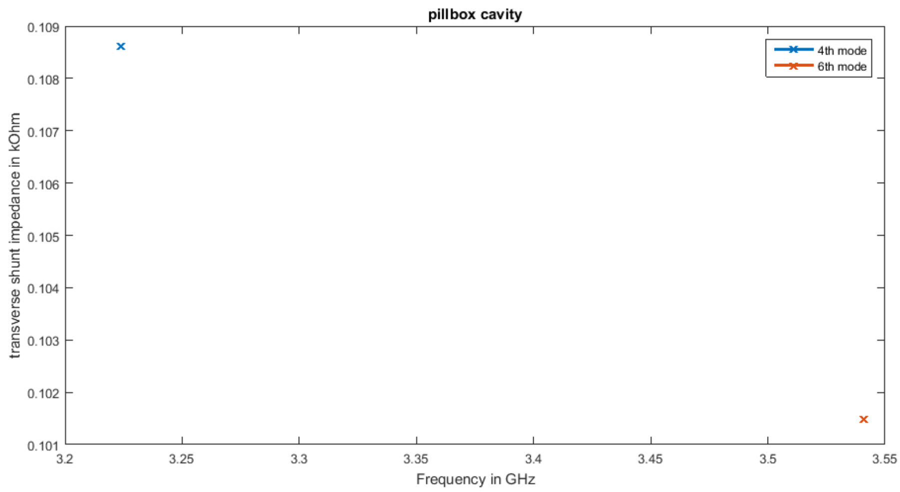

Figure 6.8. Pillbox: transverse shunt impedance eigenmode convention

The same script with opportune changes, give the results ($R^W_{s\perp}$) with the wakefield convention Figure 6.9. This one used as last check between the shunt supplied from the eigenmode and the values of the peaks (divided for the displacement) given from the wakefield simulation.

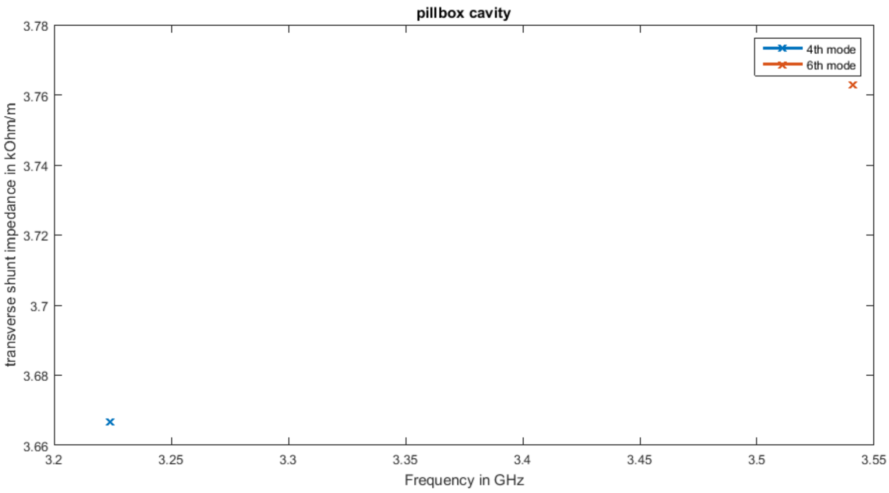

Figure 6.9. Pillbox: transverse shunt impedance wakefield convention

Is very important to see that using the wakefield convention, the transverse shunt impedance $R^W_{s\perp}$ increase more than $R^E_{s\perp}$ when the frequency increase. It is show between the chapters Figure 6.8 and Figure 6.9.

6.3 Interconnect: shunt impedance

After the detailed cross check done for the pillbox cavity, the next step has been the calculation of the shunt impedance for the FCC interconnect between two magnets at work temperature 50 K Figure 6.10. This operation has been done with the help of the scripts. In the wakefield simulations it is very hard to obtain the saturation of the peaks for high conductivity material, because the wake potential will converge at zero that is too far if there aren't a lot of losses, the wake length will be too long and the time of the simulations too. The data obtained from the post processing for the elaboration of the scrip MatLab are: Frequencies Figure 6.11, Q-factors Figure 6.12 and longitudinal shunt impedance for x Figure 6.13 and y Figure 6.14 displacements.

6.3.1 x transverse shunt impedance results

The results derived from the data above, when the beam was displaced along the x directions for the eigenmode convention Figure 6.15 and wakefield Figure 6.16 convention are showed below:

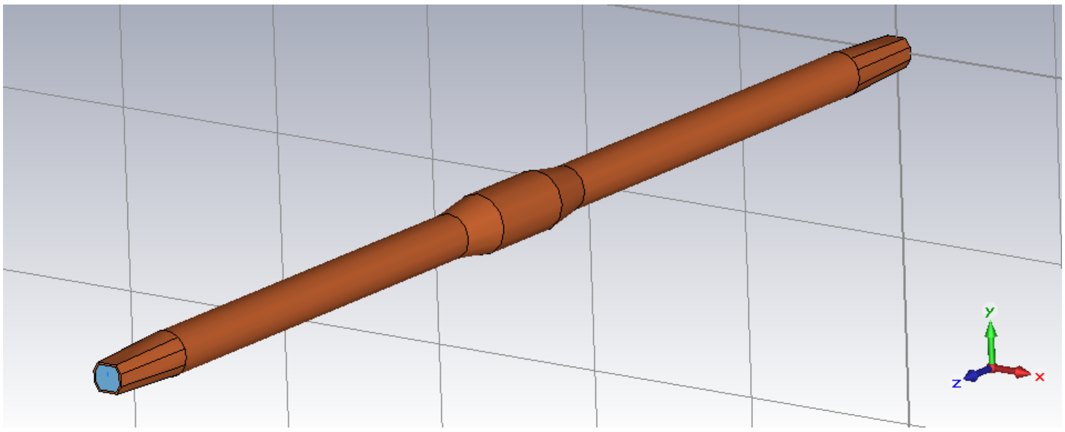

Figure 6.10. Interconnect: copper at 50 K

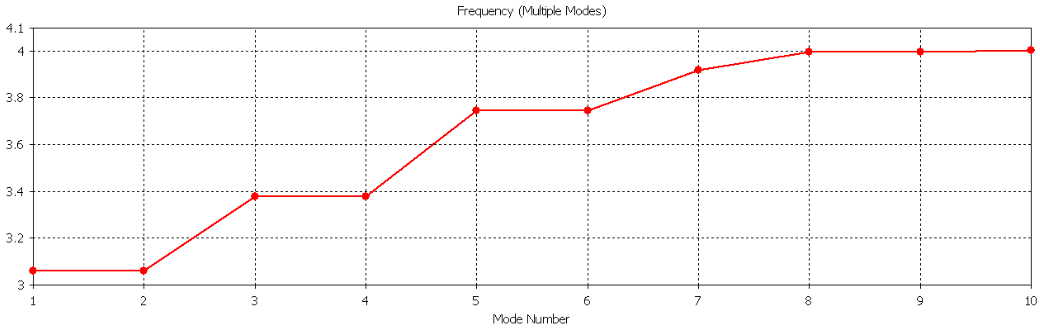

Figure 6.11. Frequencies for 10 modes

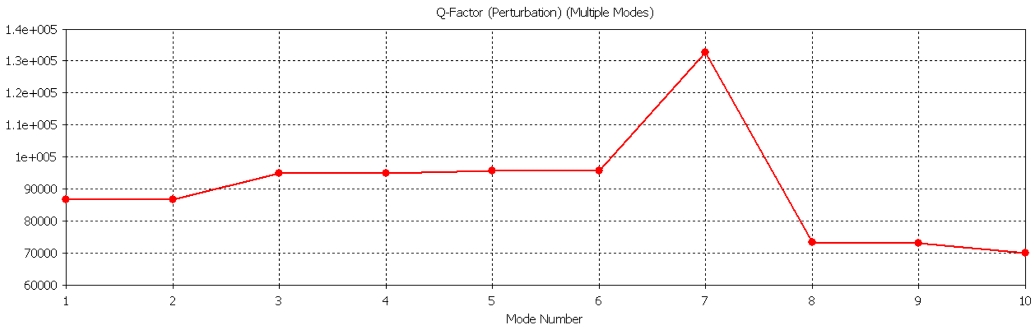

Figure 6.12. Q-factors for 10 modes

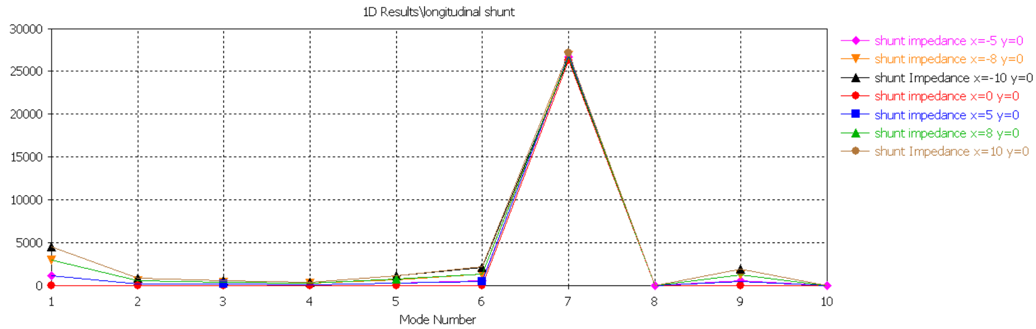

Figure 6.13. Longitudinal shunt impedance x displacements for 10 modes

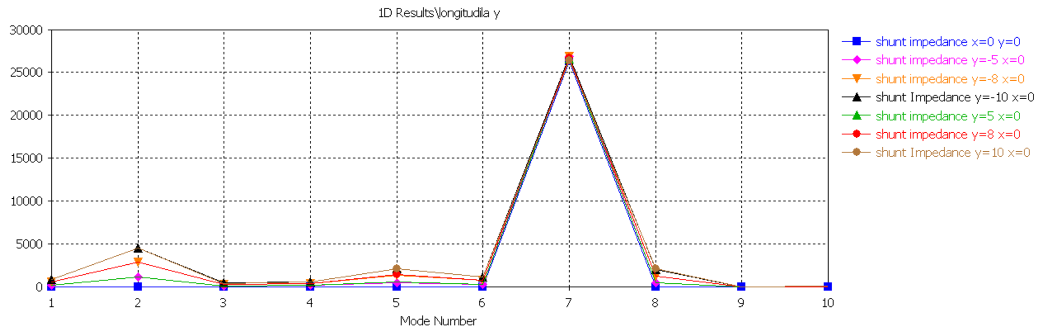

Figure 6.14. Longitudinal shunt impedance y displacements for 10 modes

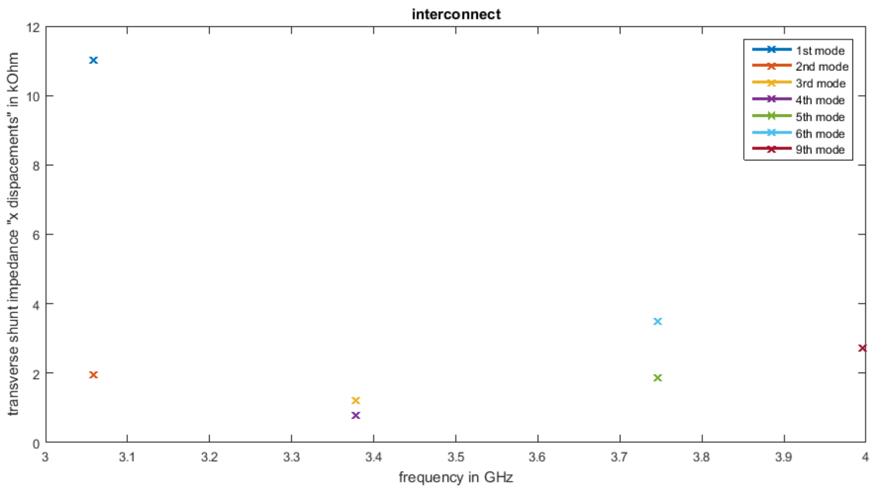

Figure 6.15. Transverse shunt impedance x displacements for 10 modes: eigenmode convention

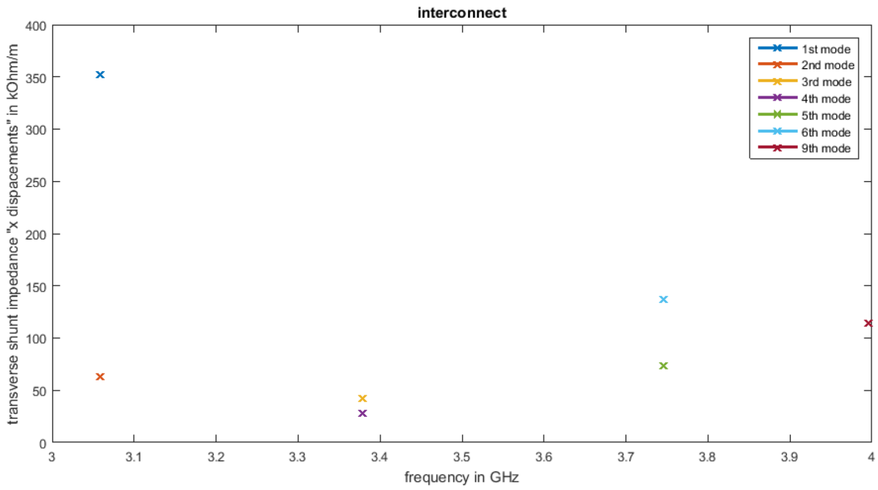

Figure 6.16. Transverse shunt impedance x displacements for 10 modes: wakefield convention

6.3.2 y transverse shunt impedance results

The results derived from the data above, when the beam was displaced along the y directions using the eigenmode convention Figure 6.17 and wakefield Figure 6.18 convention are showed below:

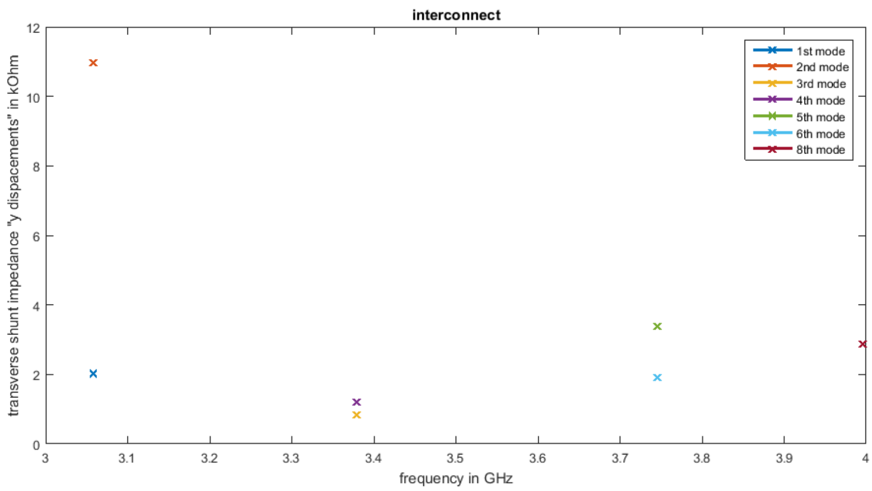

Figure 6.17. Transverse shunt impedance y displacements for 10 modes: eigenmode convention

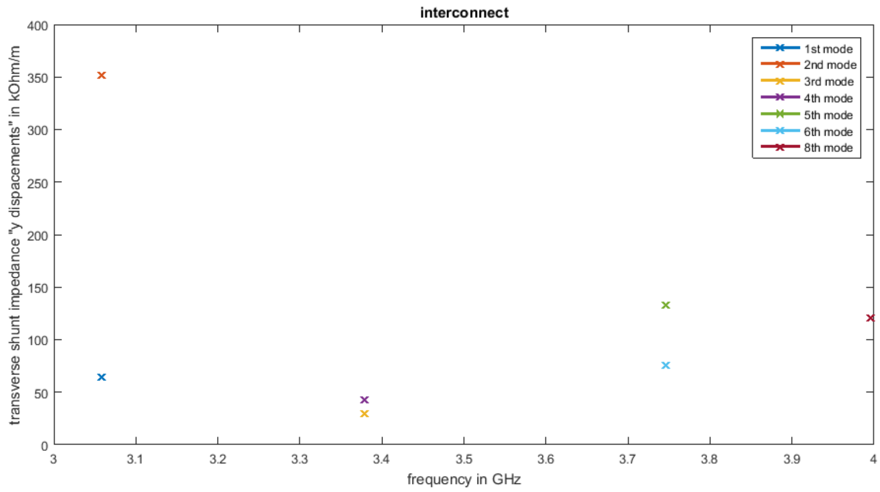

Figure 6.18. Transverse shunt impedance y displacements for 10 modes: wakefield convention

6.3.3 Considerations

Between these 10 modes the resonance frequencies that provide the transverse shunt impedance are all linked to TE modes. How said during this chapter it isn't possible for the equation (6.18) when $E_{\parallel} = 0$, but in this case, like in the case of the pillbox cavity, the transition "Figure 6.19, Figure 6.20" between cavity and pipes, with the boundary condition that for a PEC material (like is almost the copper at 50 K) the electric filed is perpendicular at the surface, therefore there will be a component $E_{\parallel} \neq 0$ and a transverse impedance as well. The confirmation that the value of the transverse shunt impedance depend from the polarity of the resonance wave, as wrote during the chapter, is shown in the charts of the results Figure 6.16 and Figure 6.18. In fact the first polarity of the electric field for the first mode, in the eigenmode solutions, is along x, so the value for the first mode of transverse shunt impedance is higher in Figure 6.16 than Figure 6.18. Is the inverse for the second mode where the polarity of the wave is along y.

6.4 Conclusions in terms of impedance

In resonance condition when $f = f_{res}$, considering the transverse shunt impedance defined in the electric equivalent circuit like (6.7), precisely for the first resonance mode where $f_{res} = 3.058\ GHz$ taken in the chapter 3. The transverse impedance value for this fixed frequency is equal the transverse shunt impedance value, it is in the worst condition using the wake convention $R^W_{s\perp} = 350\ \frac{k\Omega}{m}$ for one interconnect. The total contribution in the FCC is $R^W_{s\perp tot} = 0.35 \cdot 10^6 \cdot 4000 = 1.4\ \frac{G\Omega}{m}$. In the graph Figure 6.21 (the beam screen and collimators impedance model were made by David Amorim) it is possible to see the transverse impedance absolute values for the whole FCC, where the broad-band value for the interconnects is equal at

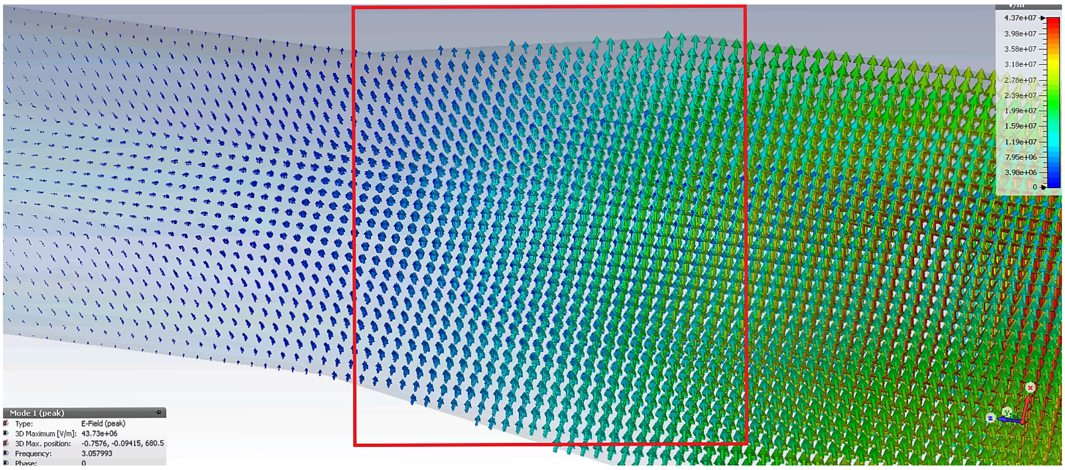

Figure 6.19. Electric field transition 1^{st} mode

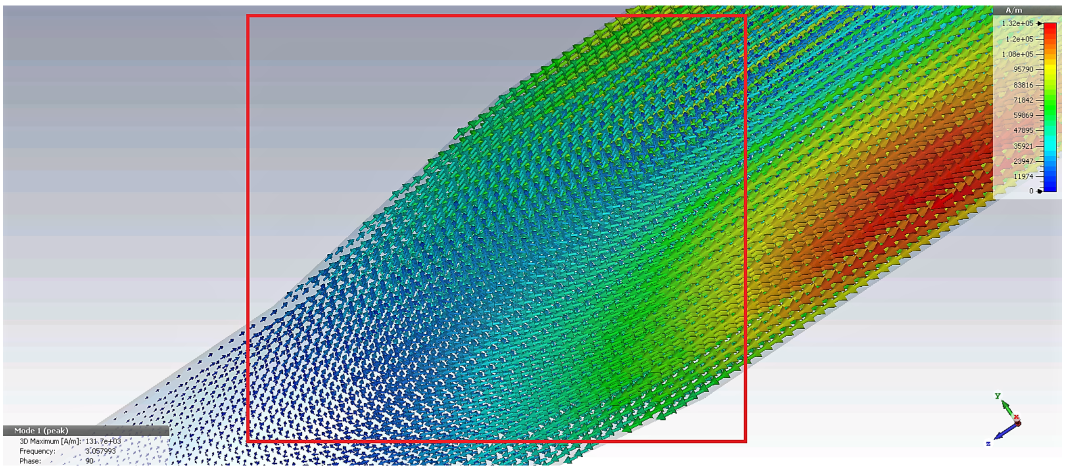

Figure 6.20. Magnetic field transition 1^{st} mode

the imaginary part it self, because the real part is zero. In addition there is the impedance value for the first resonant mode that is larger than all other trends, it could bring issues in terms of losses and successively also in beam stability in the FCC.

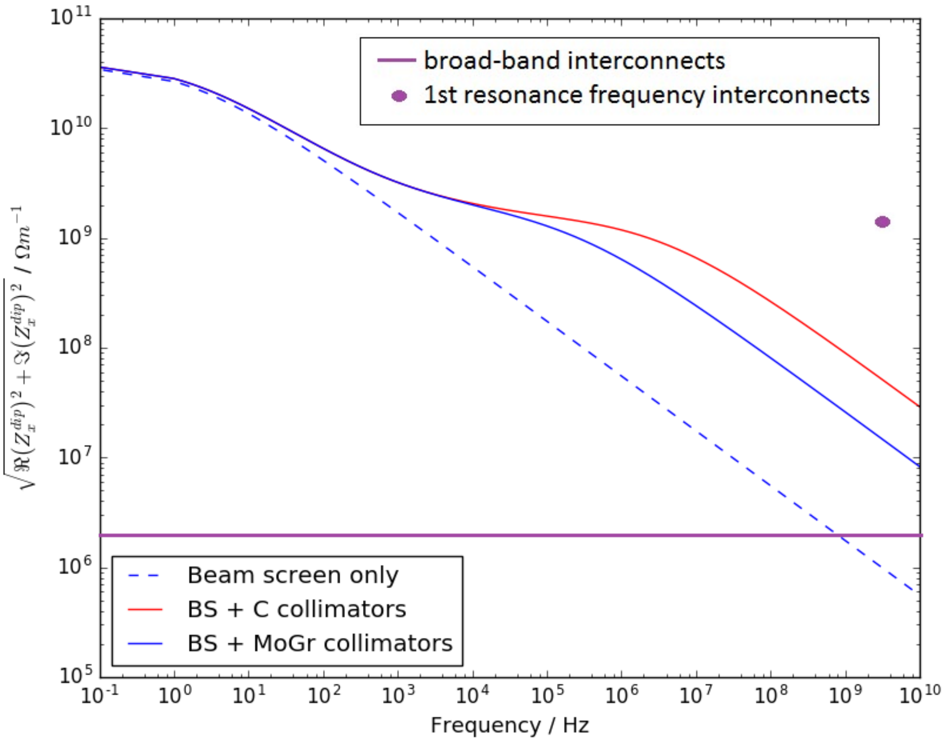

Figure 6.21. 1^{st} FCC impedance model: resonant mode impact

Chapter 7

Copper resistivity at $T = 50\ K$, observations

During the whole work over the FCC interconnect a brief period has been dedicated at a check of the electric resistivity for low temperatures. Because for a first moment the electric resistivity value for the beam screen copper used $\rho_{50K} = 0,75\Omega m$ in all past simulations wasn't suitable, value took in an Excel data sheet based over a not practical theory for the resistivity values a low temperatures [12]. This absence brought a deep study looking for the electric resistivity value, thanks to different data a value of resistivity at $T = 50\ K$ has been found.

7.1 Used data

The starting data of this study are Figure 7.1 values took from past works ([13], [14]), and other data from an excel sheet, where there are real and several resistance measurements of copper for a big temperature range: Figure 7.2 and in logarithmic scale Figure 7.3.

ρ_{300K}	ρ_{20K}	RRR_{20K}
$1{,}7 \cdot 10^{-8}$	$2{,}4 \cdot 10^{-10}$	70

Figure 7.1. Resistivity data sheet

7.2 Resistivity value a $T = 50\ K$

Using four different resistance columns measured in the Excel data sheet, normalising these values for R_{20K} i.e. like $\frac{R}{R_{20K}}$, knowing that $\frac{R}{R_{20K}} = \frac{\rho}{\rho_{20K}}$ the "residual resistance ratio" $RRR_{20K} = \frac{\rho_{300K}}{\rho_{20K}}$ was found. In particular the average between the RRR_{20K} for the four measurements over the same copper component, like best approximation was took. This average is $RRR_{20K} = \frac{R_{300K}}{R_{20K}} \simeq 75$ very similar to the value in the data sheet Figure 7.1. The equality between these two values has been the fixed point for the study. Done the hypothesis that the RRR_{50K} even was equal, its value

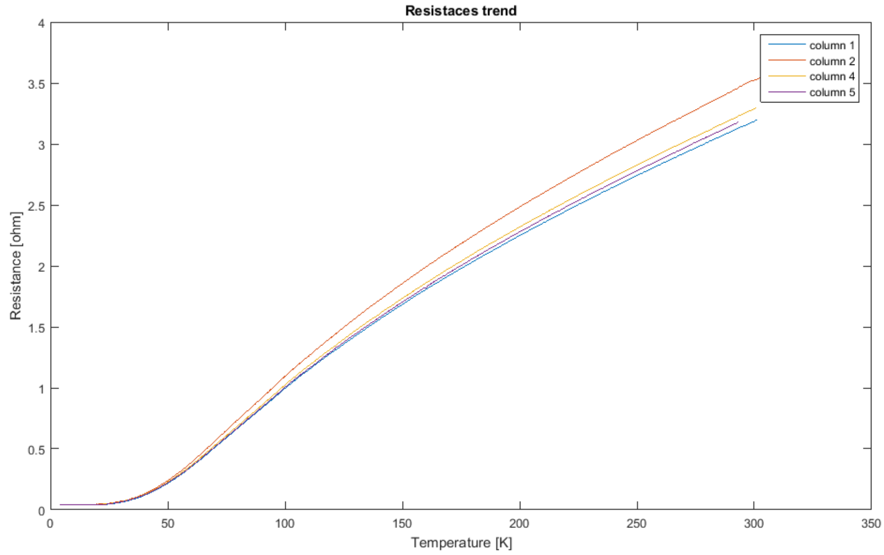

Figure 7.2. Copper: resistance measurements linear scale

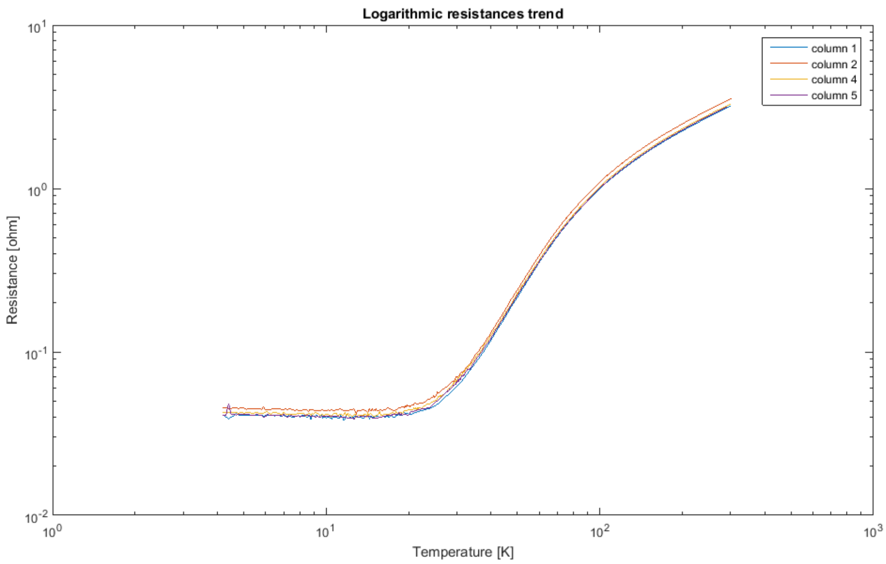

Figure 7.3. Copper: resistance measurements logarithmic scale

was calculated like average in the Excel sheet for the four measurements as well for RRR_{20K}. It is $RRR_{50K} = \frac{R_{300K}}{R_{50K}} = 14,74$. Now the value looking for which the residual resistance ratio definition was calculated (7.1):

$$\rho_{50K} = \frac{\rho_{300K}}{RRR_{50K}} = \frac{1,7 \cdot 10^{-8}}{14,74} = 1,15 \cdot 10^{-9} \tag{7.1}$$

Remembering that the value given from the theory used for the copper FCC screen is $\rho_{50K} = 0,75 \cdot 10^{-9}$, almost the half.

7.2.1 Reconstruction of the linear trend

All the resistances for the different columns Figure 7.2 have been normalised like (7.2), because the linear zone is all reported at $T = 293\ K$. The relation between resistivity and temperature for the range $T \in (173,15\ ,\ 423,15)\ K$ was shown below (7.3):

$$ratio = \frac{R}{R_{293K}} = \frac{\rho}{\rho_{293K}} \tag{7.2}$$

$$\frac{\rho}{\rho_{293}} = 1 + \alpha \Delta T \tag{7.3}$$

Knowing that $\frac{R}{R_{293}} = \frac{\rho}{\rho_{293K}}$ fixed a value of R for the different columns around the same temperature for minimise the error, the average between the different α, $\alpha = 0,002767$ was the best approximation. With the last value found the ρ_{293} used the formula (7.3) was deduced, $\rho_{293} = 1,67 \cdot 10^{-8}$. The line fit in the linear trend was reconstructed Figure 7.4:

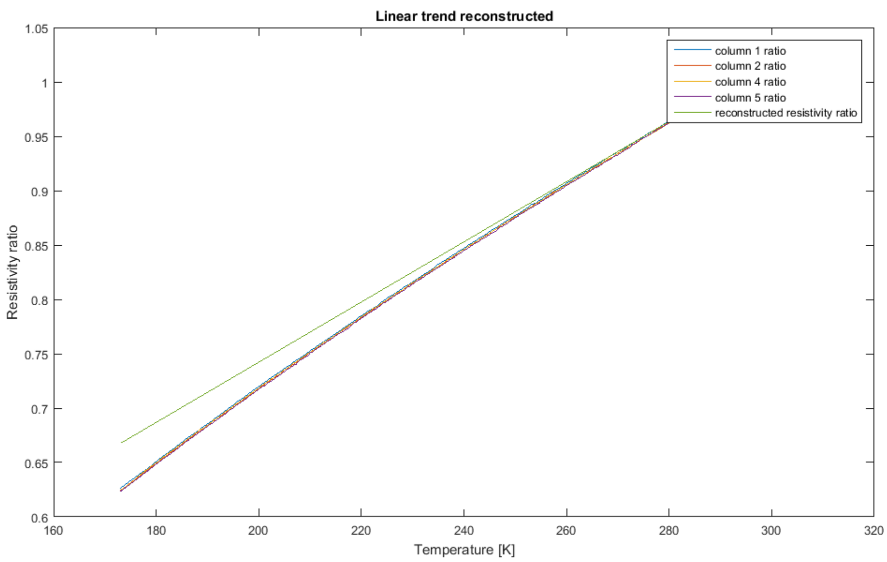

Figure 7.4. Resistivity trend in linear zone

The not perfect coupling for the temperature around $T = 173,15\ K$ is caused by the fixed value for find α took at higher temperature.

7.2.2 Reconstruction of the whole trend

Seeing during this study that the last α value is very similar at the α value for the second column of samples, and with the vary close relation for the different RRR, the amount $\rho_{293} = 1.67 \cdot 10^{-8}$ has been used to reconstruct the whole resistivity trend of the treated copper, used for the beam screen in the particle accelerators. Following the trend given from the second column thanks the ratio (7.2) multiplying all values of column for ρ_{293}, verified that all the values used and found during this work are the same. The trend is shown below Figure 7.5, in logarithmic scale Figure 7.6 and also printed over a classic chart of the copper resistivity trend Figure 7.7 found in web "https://www.copper.org/resources/properties/cryogenic/".

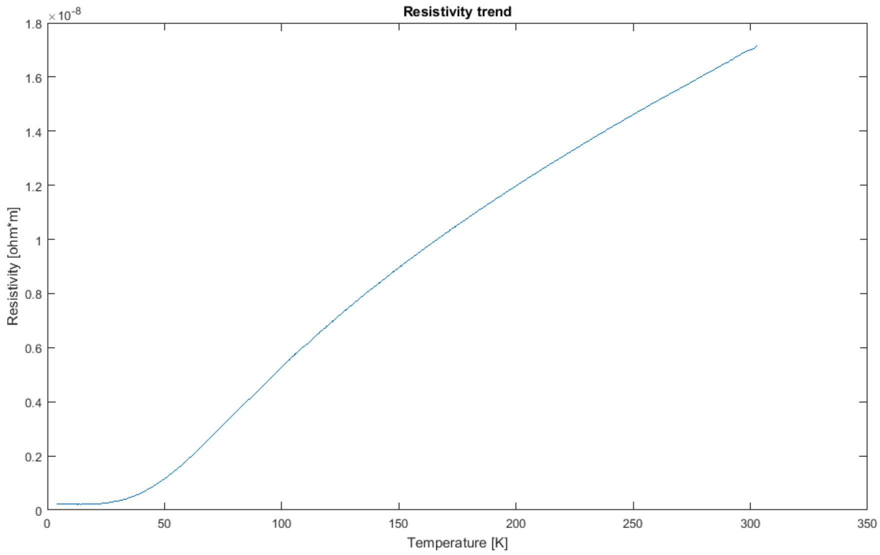

Figure 7.5. Whole resistivity trend

7.2.3 Conclusions

Is important to see that in two different resistivity cases at $T = 50\ K$ (the value given from the theory and used for all the simulations $\rho_{50K} = 0,75 \cdot 10^{-9}$ and then the value given from the study above $\rho_{50K} = 1,15 \cdot 10^{-9}$) that the Q-factors , in the same component and for the same mode, are different Figure 7.8. This inequality in the Q-factor values show the change that $\rho_{50K} = 0,75 \cdot 10^{-9}$ causes in several values inside this thesis.

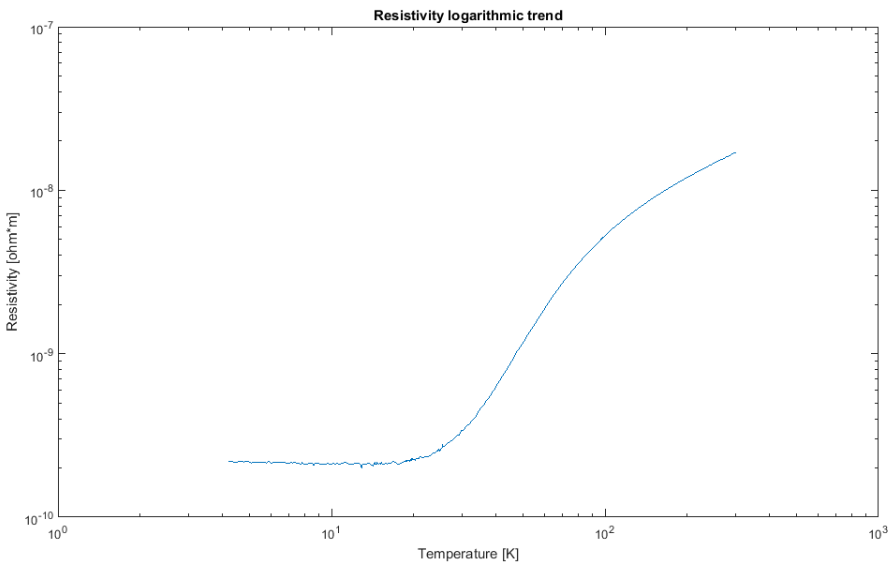

Figure 7.6. Whole resistivity trend: logarithmic scale

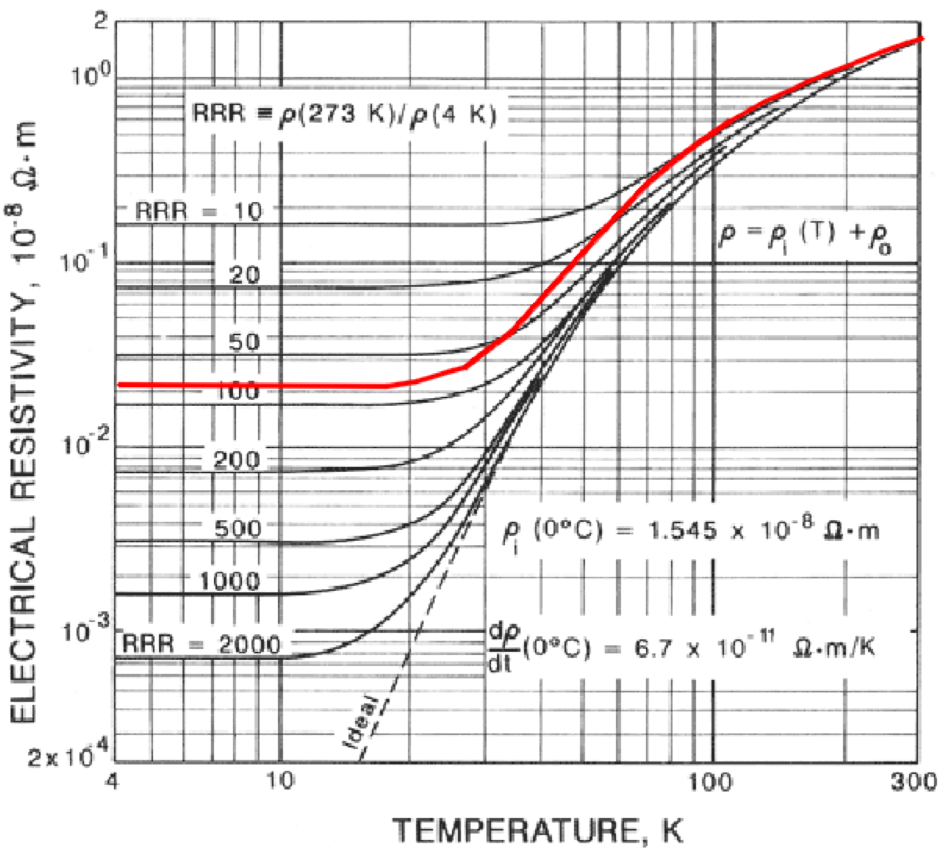

Figure 7.7. Whole resistivity trend: superimposed at a classic copper resistivity chart

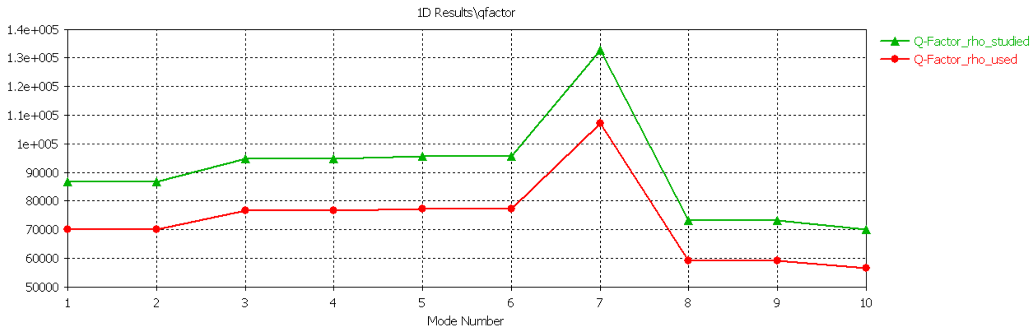

Figure 7.8. Comparison between the interconnect Q-factors at $T = 50\ K$

Chapter 8

LHC-TCDQ impedance measurements

My work at the CERN lab has been divided in two different parts. The first period focused on a research study about the FCC, with the help of theoretical bases and several simulations as is possible to see from the previous chapters. During the last month instead, a component used during several months in the LHC has been changed.

8.1 Used and spare TCDQ design

Noting that this old component had a surface colour totally different since the start, we wanted to verify if also the impedance varied due to the effect of the continuum coupling with the beam. Thus cross measurements between the used block in the LHC and two spare TCDQ, never used in the machine, have been done. The devices under test "DUTs" are shown below: Figure 8.1, Figure 8.2, Figure 8.3, Figure 8.4.

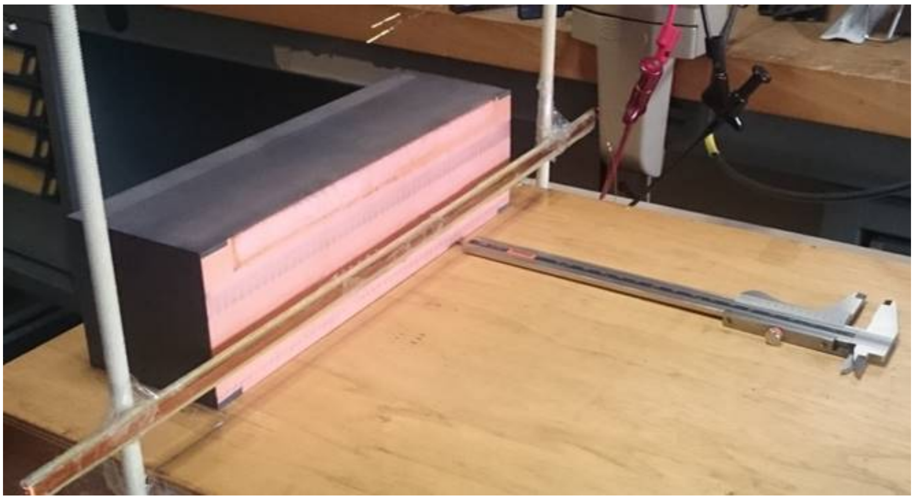

Figure 8.1. Spare TCDQ front side

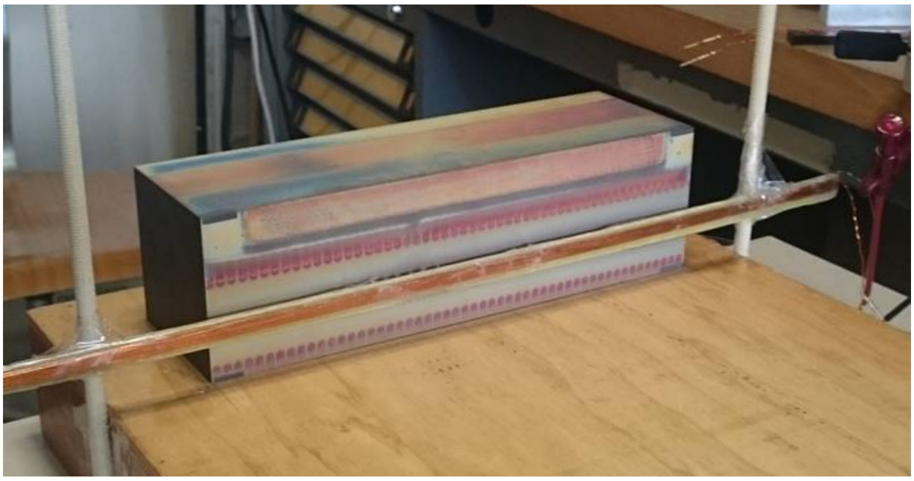

Figure 8.2. Used TCDQ front side

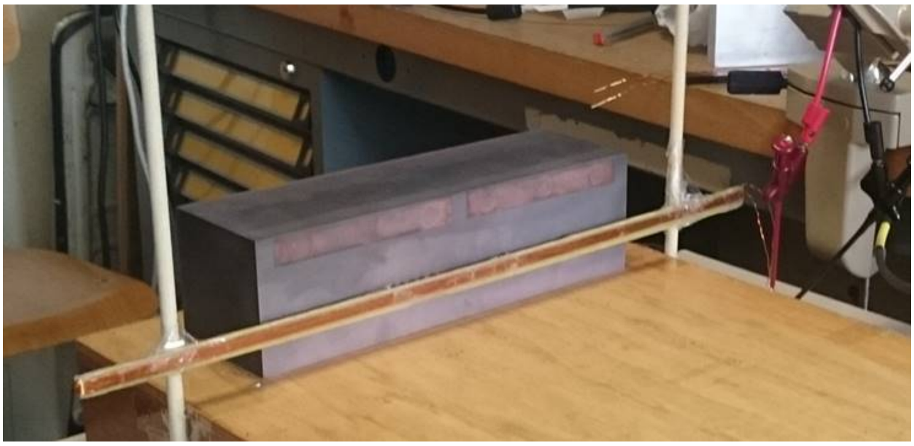

Figure 8.3. Spare TCDQ back side

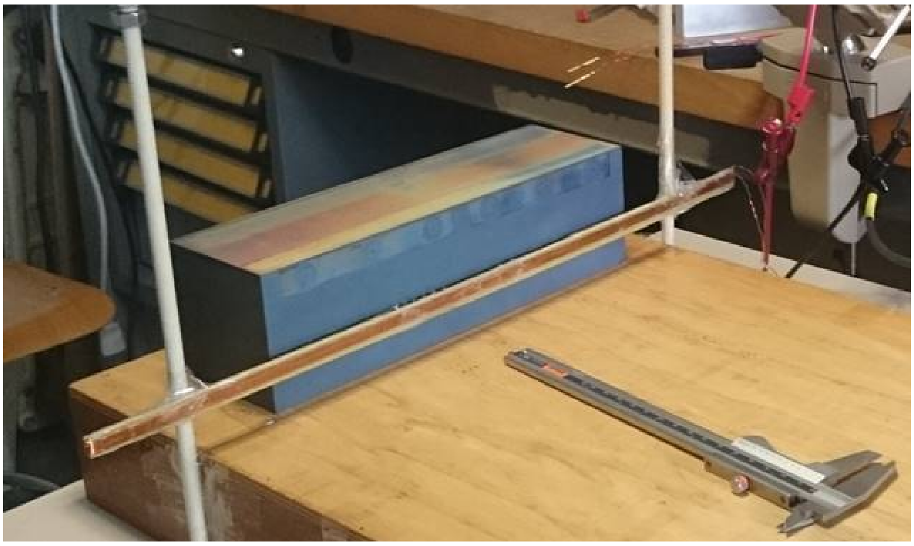

Figure 8.4. Used TCDQ back side

8.2 Used theoretical method

The dipolar transverse impedance of the DUT with a typical method of measurements for low frequencies was calculated [15], where the transverse impedance in frequency domain can be expressed in therms of electric impedance (8.1):

$$Z_{\perp}^{dip}(\omega) = \frac{c}{\omega}\frac{Z}{N^2\Delta^2} \tag{8.1}$$

In the impedance lab it was possible to measure the electric impedance of the DUT by using the S-Parameters for one port of the Network analyzer, the measurement structure has been schematised in Figure 8.5. The wire relation between S-Parameter and the electric impedance is (8.2):

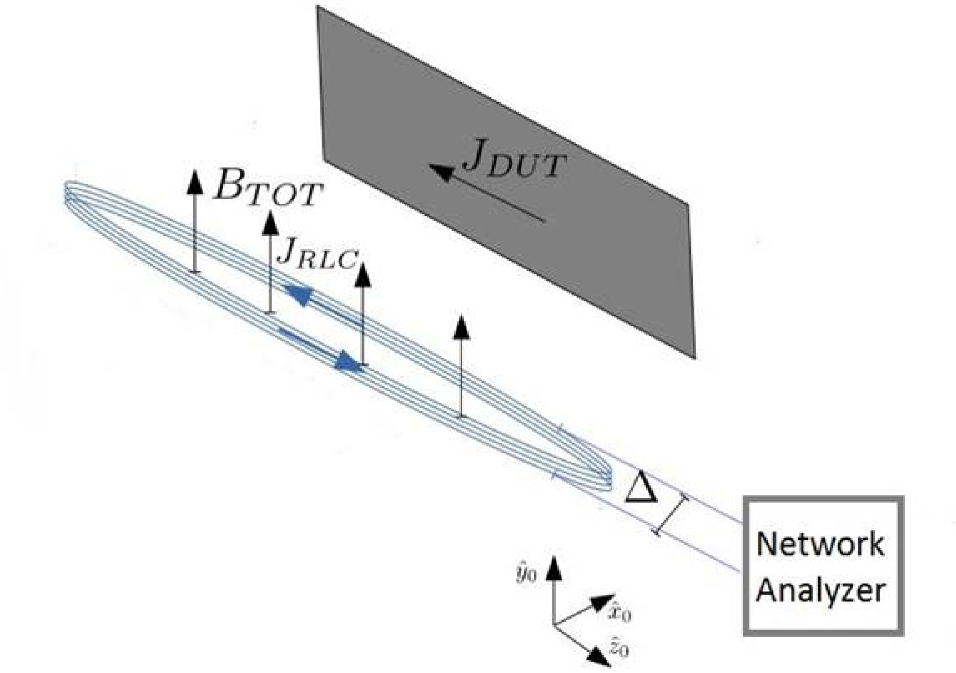

Figure 8.5. Scheme measurement structure

$$Z = Z_0\frac{1+s_{11}}{1-s_{11}} \tag{8.2}$$

Where $Z = \frac{V_1}{I_1}$ is the input impedance at port 1, N and Δ in the figure are respectively the number of the turns and the width of the antenna which represents the beam. In this type of measurements there is an issue, during them the S-Parameter has taken in account not only the DUT but also the environment. Thus by using a known "DUT reference" with the same dimensions of our DUT, it is possible to do a differential measurement that will delete the environment contribution (8.3):

$$Z_{\perp dif}^{dip}(\omega) = \frac{c}{\omega}\frac{Z^{DUT} - Z_{ref}^{DUT}}{N^2\Delta^2} \tag{8.3}$$

Where Z_{ref}^{DUT} is the impedance of the block Figure 8.7.

Figure 8.6. Reference block

8.3 Measurement structure and tools

The measurements have been done with different blocks in different displacements. The chosen reference for them was the loop centre. It was mandatory to bear in mind that it was almost impossible to determine the loop centre without touching the loop itself. The problem has been solved by using the shadow to determine the loop centre without affecting the results by touching. The other important data used for this work are shown in: Figure 8.8, Figure 8.9

8.4 Results

In lab for the measurements we had four different suitable DUTs, one reference block entirely made in aluminium Figure 8.7, two spare TCDQs called respectively TCDQU003-3 and TCDQU003-2 Figure 8.1, at the end for main block the used TCDQ called TCDQU46LB2-2 Figure 8.2. All TCDQs were characterised on the front side by a little layer of copper, followed by a thick graphite layer. The results of the differential impedances measurements were shown like cross checks between the different TCDQ. Measurements done for each block, in front and back side, for several displacements taken from the shadow loop centre. The devices in the charts were identified with their specifics names.

8.4.1 Front measurements and cross checks: charts

For the measurements in front side the results were: Figure 8.10, Figure 8.11, Figure 8.12.

Figure 8.7. Real measurement structure

N	$\Delta\ [m]$
20	$6{,}25 \cdot 10^{-3}$

Figure 8.8. Loop data sheet

$f.band\ [MHz]$	$disp.\ [mm]$
from 0 to 1	$6 - 8 - 10$

Figure 8.9. Data measurements

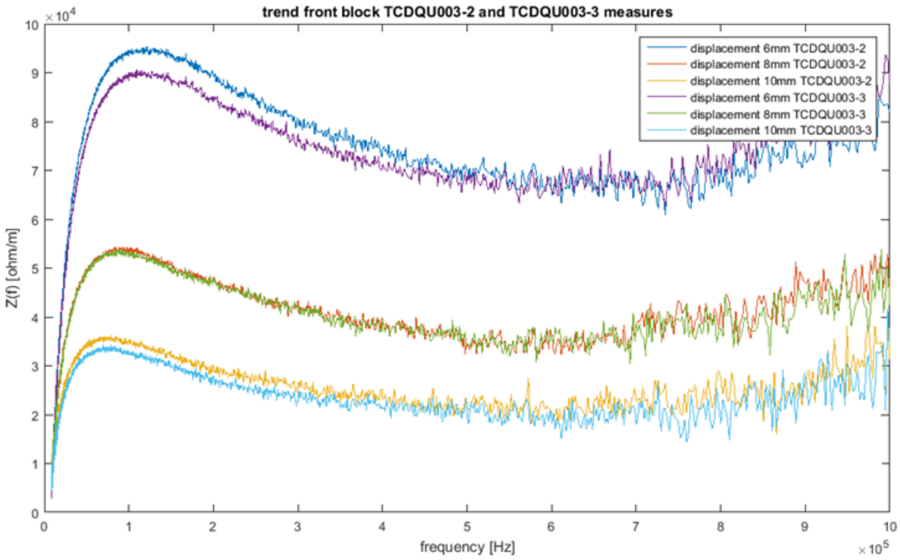

Figure 8.10. Front TCDQU003-2 and TCDQU003-3 cross check

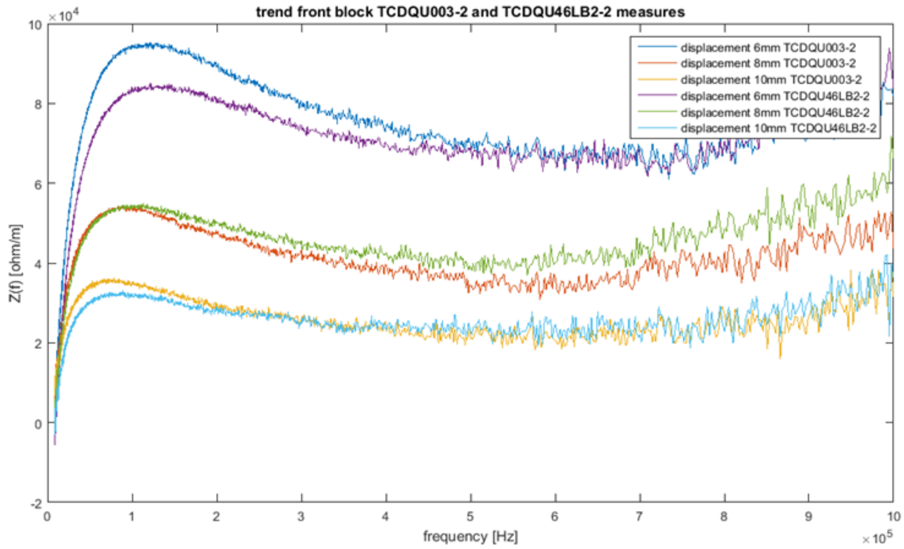

Figure 8.11. Front TCDQU003-2 and TCDQU46BL2-2 cross check

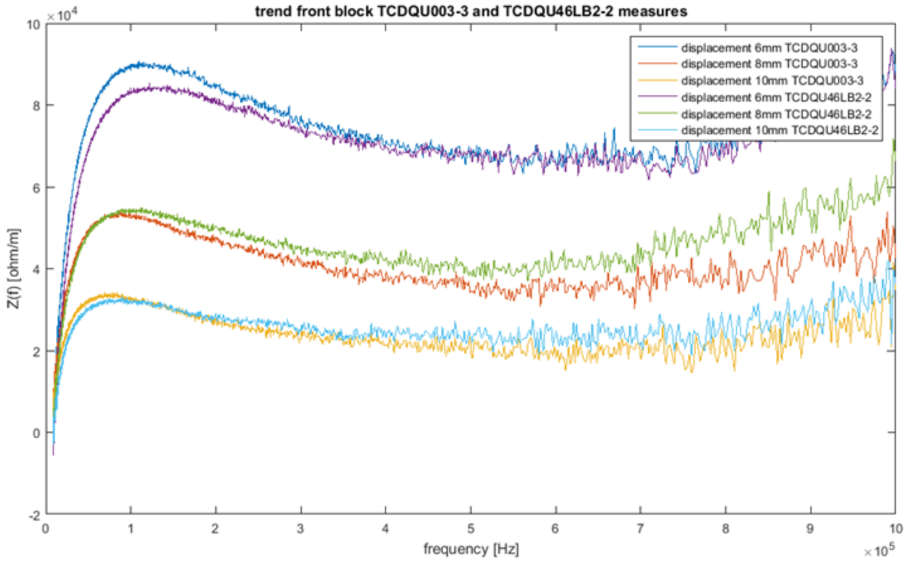

Figure 8.12. Front TCDQU003-3 and TCDQU46BL2-2 cross check

8.4.2 Back measurements and cross checks: charts

For the measurements in back side the results were: Figure 8.13, Figure 8.14, Figure 8.15.

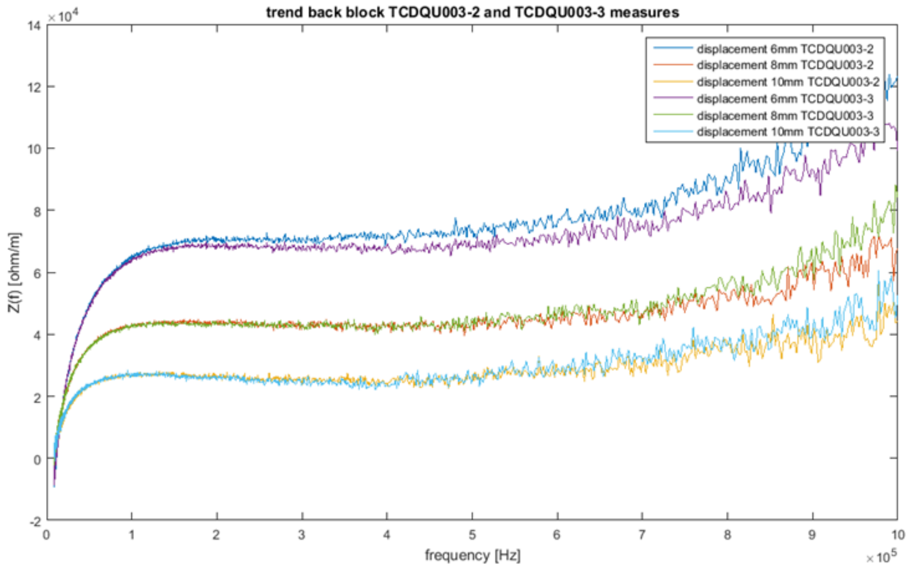

Figure 8.13. Back TCDQU003-2 and TCDQU003-3 cross check

8.5 Conclusions

It is possible to deduce from the previous graphs that the only difference between spare TCDQ and used TCDQ is the colour. After many months of operation, the

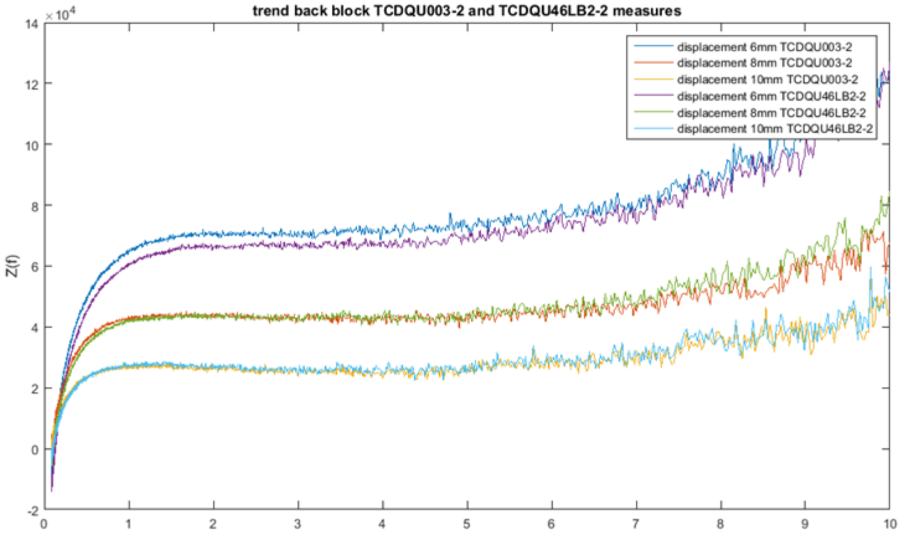

Figure 8.14. Back TCDQU003-2 and TCDQU46BL2-2 cross check

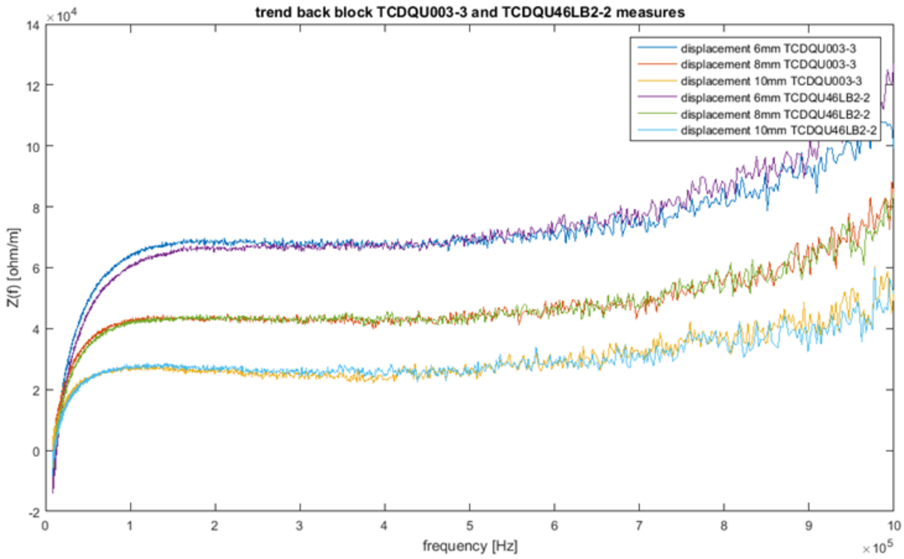

Figure 8.15. Back TCDQU003-3 and TCDQU46BL2-2 cross check

TCDQ impedance didn't show any variations and for this reason the resistivity of the coating and bulk as well.

Chapter 9

Conclusions

Conclusions The results of my work concerning the beam coupling impedance on the accelerator devices that have been examined are listed in the following:

- After several simulations and a careful research, it is possible to state that, for the analyzed frequency interval, the interconnects, still in design finalization, present a beam coupling impedance which is negligible when compared to the coupling impedance of other components that are going to be installed in the FCC. The first resonant frequency, despite the high value of shunt impedance, appears at very high frequency and does not represents, for the moment, a concern with respect to beam stability.
- Detailed studies have been done on the TCDQ collimator jaw which changed surface colour after several months of operation in the LHC. Resonant loop measurements demonstrated that the electrical resistivity, and therefore the impedance, did not change. This result is interesting for all the scientific community as the impedance of coated devices as the TCDQ, are now proven to preserve their electrical properties during long time of operation at high energies in standard conditions.

In short, my experience at CERN can be summarized through a single sentence: an “unforgettable” experience.

Bibliography

[1] M. Benedikt and F. Zimmermann, "Towards Future Circular Colliders," Dec 2015.

[2] C. Renato, "Microonde I° Modulo, appunti corso di microonde,"

[3] R. Fabrizio, "Longitudinal impedance simulations for the slots in the LHC beam screen and first applications to the HL-LHC," 2015.

[4] H. A. Day, E. Metral, and R. Jones, *Measurements and Simulations of Impedance Reduction Techniques in Particle Accelerators.* PhD thesis, Manchester U., 2013. Presented 28 Jun 2013.

[5] N. Biancacci, L. Palumbo, M. Migliorati, E. Métral, and B. Salvant, *Improved techniques of impedance calculation and localization in particle accelerators.* PhD thesis, Rome U., Apr 2014. Presented 07 05 2014.

[6] E. Métral, "Overview of Single-Beam Coherent Instabilities in Circular Accelerators," 2005.

[7] O. S. Brüning, P. Collier, P. Lebrun, S. Myers, R. Ostojic, J. Poole, and P. Proudlock, *LHC Design Report.* Geneva: CERN, 2004.

[8] M. W. F. Caspers, "JUAS RF Course 2016.," 2016.

[9] B. Salvant, L. Rivkin, and E. Metral, *Impedance model of the CERN SPS and aspects of LHC single-bunch stability.* PhD thesis, Ecole Polytechnique, Lausanne, Switzerland, 2010. Presented on 04 Mar 2010.

[10] L. Palumbo, V. G. Vaccaro, and M. Zobov, "Wake fields and impedance," p. 70 p, Sep 1994.

[11] G. Burt, "Transverse deflecting cavities," p. 11 p, Jan 2012. Comments: 11 pages, contribution to the CAS - CERN Accelerator School: Specialised Course on RF for Accelerators; 8 - 17 Jun 2010, Ebeltoft, Denmark.

[12] O. Madelung and G. K. White, *Metals: electronic transport phenomena.* Landolt-Börnstein. New series. Group 3 Crystal and solid state physics, Berlin: Springer, 1991.

[13] F. Caspers, M. Morvillo, F. Ruggiero, J. Tan, and H. Tsutsui, "Surface Resistance Measurements of LHC Dipole Beam Screen Samples," p. 4 p, Aug 2000.

[14] N. Mounet, L. Rivkin, and E. Métral, *The LHC Transverse Coupled-Bunch Instability*. PhD thesis, Ecole Polytechnique, Lausanne, Mar 2012. Presented 2012.

[15] G. Nassibian and F. J. Sacherer, “Methods for measuring transverse coupling impedances in circular accelerators,” *Nucl. Instrum. Methods*, vol. 159, no. 1, pp. 21–7, 1979.